J. Fluid Mech. (2001), *vol.* 435, *pp.* 217–246. Printed in the United Kingdom

© 2001 Cambridge University Press

On the density waves developed in gravity channel flows of granular materials

By CHI-HWA WANG AND ZIQUAN TONG

Department of Chemical Engineering, National University of Singapore,
10 Kent Ridge Crescent, Singapore 119260

(Received 29 April 2000 and in revised form 20 November 2000)

This paper provides insight to the transient development of density waves generated in gravity-driven flows of granular materials. The evolution of three modes of dominant linear instabilities (predicted in a previous work by Wang, Jackson & Sundaresan 1997) is examined by FFT analysis. For the first symmetric density wave (SDW1) mode, the evolution is governed by the linear instability. The second symmetric density wave (SDW2) mode undergoes a few stages of temporal development; as a result, large particle clusters gradually degenerate into a series of smaller clusters in the flow direction. For the anti-symmetric (ASDW) mode, the corresponding particle distribution shows significant development in the direction perpendicular to the flow. The present study indicates that the wall roughness may affect the structure of the density waves, but these density waves need not be triggered by the wall roughness. All the three modes of instabilities reported in this work are of inertial nature and occur only when the particle–particle collisions are significantly inelastic.

1. Introduction

The flow of granular materials is of great interest to scientists and engineers. The understanding of its dynamics is essential for the better design and operation of many particle-related industrial processes. Since Bagnold (1954) performed his pioneering work on the rheological behaviour of granular materials, many researchers have contributed to this subject. In recent years, several investigations have been reported in the literature regarding the flow of granular materials, both theoretical and experimental. Astarita & Ocone (1994) analysed the general characteristics theory of granular materials using large-scale statistical thermodynamics (LSST). Tan *et al.* (1995) used the lattice-Bhatnagar–Gross–Krook (BGK) model to simulate the shear flow of granular materials. Zhang & Foda (1997) used the Kelvin–Helmholtz type instability mechanism to study the sliding motion of finite depth of bulk granular materials.

Extensive work has also been reported on the gravity flow of granular materials in vertical pipes, channels and hoppers. The methodologies employed in these studies comprise the continuum approach (Goodman & Cowin 1971; Savage 1979; Nunziato & Passman 1980; Babić 1993; Wang, Jackson & Sundaresan 1997) and particle simulations (Sanders & Ackermann 1993; Lee & Leibig 1994).

Base-state solutions of the gravity channel flows have been examined over the past few decades. Savage (1979) applied a nonlinear theory to two-dimensional gravity flow of a bulk solid down a rough-walled vertical channel and derived analytical expressions for the profiles of velocity and volume fraction. In these expressions, the

https://doi.org/10.1017/S0022112001003792 Published online by Cambridge University Press

solid fraction is maximum at the centreline of the channel and decreases monotonically towards the wall. Babić (1993) applied the kinetic theory of granular materials to the problem of vertical channel flow of slightly inelastic, circular disks. The constitutive relations and boundary conditions used in his study are essentially the same as those used by Richman & Chou (1988).

In recent years, several studies have been reported on the occurrence of density waves in granular flows. Sanders & Ackermann (1991, 1993) carried out particle dynamics simulations for two-dimensional disks in an inclined channel. These flows produced slugs or regions along the channel characterized by the occurrence of densely packed groups of flowing disks. The non-uniformity of the flow (the occurrence of slugs) increased as the disks were made more inelastic.

Lee (1994) studied density waves in the flows of particles through vertical tubes using both analytical methods and molecular dynamics simulations. The equations of motion for quasi-one-dimensional systems, combined with Bagnold's law for the 'grain-inertia' regime, were used to describe the time evolution of the density and velocity fields for narrow tubes. He showed that kinetic waves exist and obtained the condition for dynamic waves from the model. Peng & Herrmann (1994, 1995) used lattice-gas automata to model the formation of density waves of granular flow. They found that the spontaneous density waves propagate through the vertical pipe with well-defined shapes and velocities. They concluded that both the dissipation and roughness factors are essential for the emergence of these density waves.

Lee & Leibig (1994) used molecular dynamic simulations and found a density pattern in a vertical pipe, in which a number of regions with high density are separated from each other by regions of low density. Bolio & Sinclair (1995) studied the gas turbulence in the pneumatic conveying of massive particles in vertical tubes. Tan *et al.* (1995) applied the lattice-BGK approach to simulate shear flow of granular materials. They could reproduce and examine the phenomenon of 'clustering instability', the spontaneous agglomeration of particles into dense clusters. Riethmuller *et al.* (1997) used a Langvin formulation to study the gravity-driven flow of granular materials through a rough and narrow vertical pipe. They found that the homogeneous flow becomes unstable with respect to short-wavelength perturbations. Wang *et al.* (1997) investigated the gravity-driven flow of granular materials in a vertical channel. Based on a continuum rheological model proposed by Lun *et al.* (1984), they examined the structure of instabilities and the condition at which a gravity flow loses its stability. They found three modes of travelling wave instabilities with instabilities occurring only with the significantly inelastic particle–particle collisions.

In recent years, besides abundant simulation studies, a few experimental studies on gravity-driven flows have also been carried out. Horikawa *et al.* (1996) carried out such experiments through a vertical glass pipe by draining granular materials from a hopper. They found a few self-organized critical density waves and these are believed to be due to the back-flow of air. Nakahara & Isoda (1997) investigated density fluctuations of metallic spheres falling through a vertical glass pipe filled with liquid. They observed that above a certain packing rate, metallic spheres form slugs and slowly fall into groups. At the 'slugging' transition point, the power spectrum of the density fluctuation obeys a power law with a negative exponent.

From the previous work reported in the literature, it is confirmed that density waves do exist under certain conditions in granular material flows. However, the mechanism for triggering the formation of these waves is not clear, and nor is the temporal evolution of the flow and density fields if randomly generated perturbations are added to the system. It is also interesting to examine if the pattern developed has any

https://doi.org/10.1017/S0022112001003792 Published online by Cambridge University Press

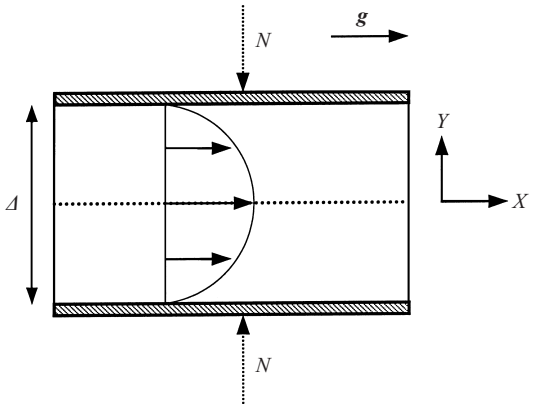


FIGURE 1. Schematic diagram of the granular flow in a vertical channel showing the velocity distribution at a given cross-section, $\boldsymbol{g}$ is the specific gravity force.

resemblance to the dominant instability predicted by the linear theory. This work is of interest as it is the first integration of a set of continuum equations for a rapid flow of granular material under gravity. Considering collisions to be the main means of momentum transfer across the channel, the present study examines whether complicated density waves can indeed be triggered solely by the interactions between particles and between particle and the wall. All these points are addressed in the present work.

2. Governing equations

The gravity-driven flow of granular materials is confined between two vertical infinite plates as shown in figure 1. Cartesian coordinates are set up with the origin in the central plane, the x-axis vertical (parallel to the gravitational acceleration) and the y-axis normal to the two bounding plates, which are stationary and separated by a distance Δ. The constant distance between the two plates is maintained by applying a normal stress N to prevent them from being pushed apart by the impact of the flowing granular materials. The equations of motion are those used in Wang *et al.* (1997), comprising the following continuity, momentum, and pseudo-thermal energy balance equations:

$$\frac{\partial v}{\partial t} + \nabla \cdot (v\boldsymbol{u}) = 0, \tag{1}$$

$$\rho_s v \frac{\mathrm{D}\boldsymbol{u}}{\mathrm{D}t} = -\nabla \cdot \boldsymbol{\sigma} + \rho_s v \boldsymbol{g}, \tag{2}$$

$$\frac{3}{2}\rho_s v \frac{\mathrm{D}T}{\mathrm{D}t} = -\nabla \cdot \boldsymbol{q} - \boldsymbol{\sigma} : \nabla \boldsymbol{u} - J. \tag{3}$$

Here v denotes the volume fraction of particles; $\boldsymbol{u}$ is the local-average velocity of the particles; ρ_s is the density of the particles; $\boldsymbol{\sigma}$ is the compressive stress tensor; T is the granular temperature, defined as $(1/3)\langle u'^2 \rangle$, where u' is the magnitude of the fluctuation about the local mean velocity; $\boldsymbol{q}$ is the flux vector of the pseudo-thermal energy associated with the fluctuations in particle velocity; and J denotes the rate of dissipation of this energy, per unit volume, by inelastic collisions between particles.

The constitutive relations for $\boldsymbol{\sigma}$ can be found elsewhere (Wang *et al.* 1997; Wang & Tong 1998; Nott *et al.* 1999). These relations are based on the earlier work by Hui *et al.* (1984), Johnson & Jackson (1987), and Lun *et al.* (1984). The constitutive

https://doi.org/10.1017/S0022112001003792 Published online by Cambridge University Press

relations for $\boldsymbol{\sigma}$, $\boldsymbol{q}$, and J have been developed by Lun *et al.* (1984):

$$\boldsymbol{\sigma} = [\rho_s v T(1+4\eta v g_0) - \eta\mu_b \nabla\cdot\boldsymbol{u}]\boldsymbol{I} - 1.2\left\{\frac{2\mu}{\eta(2-\eta)g_0}(1+\tfrac{8}{5}v\eta g_0)[1+\tfrac{8}{5}\eta(3\eta-2)vg_0]+\tfrac{6}{5}\mu_b\eta\right\}\boldsymbol{S}, \tag{4}$$

$$\boldsymbol{q} = \frac{-\lambda}{g_0}\left\{(1+\tfrac{12}{5}\eta v g_0)[1+\tfrac{12}{5}\eta^2(4\eta-3)vg_0]+\frac{64}{25\pi}(41-33\eta)(\eta v g_0)^2\right\}\nabla T - \frac{\lambda}{g_0}\frac{12}{5}\eta(\eta-1)(2\eta-1)[1+\tfrac{12}{5}\eta v g_0]\frac{\mathrm{d}}{\mathrm{d}v}(v^2 g_0)\frac{T}{v}\nabla v, \tag{5}$$

$$J = \frac{48}{\pi^{0.5}}\eta(1-\eta)\frac{\rho_s v^2}{d}g_0 T^{1.5}, \tag{6}$$

where $\boldsymbol{S}$ is the deviatoric part of the rate of deformation:

$$\boldsymbol{S} = \tfrac{1}{2}(\nabla\boldsymbol{u} + \nabla\boldsymbol{u}^T) - \tfrac{1}{3}(\nabla\cdot\boldsymbol{u})\boldsymbol{I},$$

$\eta = (1+e_p)/2$, where e_p is the coefficient of restitution for collisions between particles, while the two viscosity factors μ and μ_s, and the thermal conductivity factor λ, are given by

$$\mu = \frac{5M(T/\pi)^{0.5}}{16d^2}, \quad \mu_b = \frac{256\mu v^2 g_0}{5\pi}, \quad \lambda = \frac{75M(T/\pi)^{0.5}}{8\eta(41-33\eta)d^2},$$

where M and d are the mass and diameter of a particle, respectively. For g_0, which is a function of v, the form used by Johnson & Jackson (1987) is chosen, namely

$$g_0(v) = \frac{1}{1-(v/v_m)^{1/3}},$$

where v_m is the random close packing solid fraction (= 0.65).

We now restrict attention to the geometry of figure 1 and to motions confined to the (x, y)-plane. The various dimensionless variables used in this work are defined as follows:

$$u^* = u/(g\Delta)^{0.5}, \quad T^* = \rho_s T/N, \quad (X, Y) = (x, y)/\Delta, \quad \tau = t(g/\Delta)^{0.5}, \tag{7}$$

where u and v are the x and y components of the velocity, respectively.

Boundary conditions in the present study for the momentum and energy transfer at the walls are the same as those used by Johnson & Jackson (1987):

$$\boldsymbol{t}\cdot\boldsymbol{\sigma}\cdot\boldsymbol{n} = -\left(\frac{\pi\sqrt{3}}{6v_m}\right)\phi'\rho_s v g_0 T^{1/2}u_{sl}, \tag{8}$$

$$\boldsymbol{n}\cdot\boldsymbol{q} = \left(\frac{\pi\sqrt{3}}{6v_m}\right)\phi'\rho_s v g_0 T^{1/2}u_{sl}^2 - \left(\frac{\pi\sqrt{3}}{4v_m}\right)(1-e_w^2)\rho_s v g_0 T^{3/2}, \tag{9}$$

where ϕ' is a specularity factor (which measures the fraction of the momentum of an incident particle in the direction of slip which is transmitted, on average, to the wall during collision), $\boldsymbol{t}$ is a unit vector tangent to the wall, in the direction of the slip velocity, and $\boldsymbol{n}$ is the unit vector normal to the wall. The slip velocity u_{sl} is the velocity of the granular material in contact with the wall and e_w is the coefficient of restitution for particle–wall collisions.

The steady-state solutions for different values of $\bar{v}$ and Δ/d have been developed by Wang (1995) and the results are shown in figure 2 (adiabatic wall condition).

https://doi.org/10.1017/S0022112001003792 Published online by Cambridge University Press

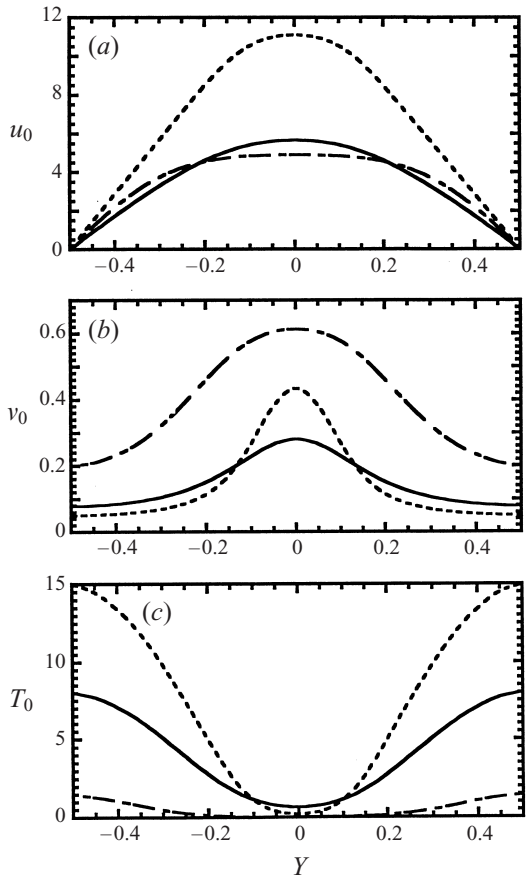


FIGURE 2. Base-state solutions of (*a*) u_0, (*b*) v_0 and (*c*) T_0 for ——, $(\bar{\nu}, \Delta/d) = (0.15, 33.3)$; – – ––, $(\bar{\nu}, \Delta/d) = (0.40, 33.3)$ and – – – –, $(\bar{\nu}, \Delta/d) = (0.15, 66.6)$.

The base-state distribution of particles across the width of the channel is found to be non-uniform and a dense plug develops at the centre with large plate separations. The volume fraction of solids (ν_0) decreases monotonically from the centre of channel to the walls for the case of adiabatic walls. These characteristics are qualitatively similar to those predicted by Babić (1993) for gravity-driven flows of smooth, inelastic disks between parallel bumpy boundaries. The temporal evolution of the unstable modes is examined by adding small perturbations to a base state (u_0, v_0, T_0) as follows:

$$u^* = u_0(Y) + u', \tag{10a}$$

$$v^* = v', \tag{10b}$$

$$\nu = \nu_0(Y) + \nu', \tag{10c}$$

$$T^* = T_0(Y) + T', \tag{10d}$$

where

$$u' = u_e(Y)\exp(\Omega\tau)\exp(\mathrm{i}K_x X), \tag{11a}$$

$$v' = v_e(Y)\exp(\Omega\tau)\exp(\mathrm{i}K_x X), \tag{11b}$$

$$\nu' = \nu_e(Y)\exp(\Omega\tau)\exp(\mathrm{i}K_x X), \tag{11c}$$

$$T' = T_e(Y)\exp(\Omega\tau)\exp(\mathrm{i}K_x X). \tag{11d}$$

https://doi.org/10.1017/S0022112001003792 Published online by Cambridge University Press

Here Ω is the complex growth rate and K_x is the dimensionless wavenumber in the direction of flow. The dimensionless phase velocity is given by $-\Omega_i/K_x$.

3. Dominant density-wave instabilities

According to Wang *et al.* (1997), three types of travelling wave instabilities (namely SDW1, SDW2 and ASDW) were observed. The classification of different modes of instabilities is based on the nature of the corresponding density wave. Here, the terms SDW and ASDW are respectively used to refer the density eigenfunction either symmetric or antisymmetric about the centreline of the vertical channel. The detailed structure of each mode will be shown in the subsequent sections. These three modes of dominant instabilities are characterized by their own intrinsic values of wavenumber (K_x), growth rate (Ω_r) and phase velocity ($-\Omega_i/K_x$). In order to maintain consistency with the literature, the notations for different modes are retained in this paper. The dimensionless parameters which determine the dominant mode comprise the average solid fraction ($\bar{v}$) and the plate separation (Δ/d).

The main objective of this work is to investigate the fate of a density field subjected to infinitesimal perturbations in the SDW1, SDW2 and ASDW modes. This is tracked through the transient integration of the macroscopic balance equations and examined by a fast Fourier transform (FFT) analysis. The density patterns reported in this work represent the three possible dominant modes in the stability diagram, as observed by Wang *et al.* (1997). We have made no attempt to separate the three dominant modes artificially. Instead, efforts have been made to examine the individual development of each of the three modes. Although the three density patterns are the dominant modes at various conditions (solid fraction, plate separation, etc), we cannot rule out the possibility that the interactions among these modes and the base flow may be important past the initial linear growth. However, how can one determine the importance of this aspect without a clear picture of the transient development of each individual mode? The clarification of this picture is the aim of the present study.

The transient integration of the macroscopic governing equations is performed using a finite-element method. The length and width of the computational domain are taken as the characteristic dimensional wavelength (λ_x) in the flow direction and the plate separation (Δ), respectively. Hence, the computational length for different modes of instabilities is estimated from their dominant wavenumber K_x ($K_x = 2\pi/(\lambda_x/\Delta)$). The simulation code captures the existing least-stable mode and then perturbs the base-state flow field accordingly. The parameter values used in the analysis for the SDW1, SDW2 and ASDW modes are summarized in table 1 and the resulting temporal evolution of density waves is discussed in the subsequent sections. The key steps involved in the numerical methods for the eigenvalue and transient analyses are provided in the Appendix. The finite-element formulation involves a rectangular grid mesh with a typical 1260×1260 matrix equation solved by various standard mathematical software packages. The spatial and temporal convergence has been examined by varying the time step and the grid sizes respectively to ensure the convergence falling within $\pm 0.01\%$.

The FFT is performed using *Matlab* and the analysis is carried out with only the signals of the first two quadrants in the wavenumber space, due to the symmetrical properties of the FFT (Dudgeon & Mersereau 1984). In all the sections, the results of an adiabatic-wall condition ($e_w = 1, u_{sl} = 0$) are used, except in the last section, where both the effect of the wall boundary condition and the mechanism of instabilities are addressed.

https://doi.org/10.1017/S0022112001003792 Published online by Cambridge University Press

Parameter	SDW2	SDW1	ASDW
Δ/d dimensionless channel width	33.3	33.3	66.6
$\bar{\nu}$ average solid fraction	0.15	0.40	0.15
K_x dimensionless wavenumber in the flow direction	0.52	0.17	4.6
U_w scale for velocity, $U_w = (g\Delta)^{1/2}$ (m s^{-1})	0.77	0.77	1.08
T_s scale for temperature, $T_s = N/\rho_s$ (m^2 s^{-2})	1447	4304	3110
ρ_s solid material density (kg m^{-3})	2980	2980	2980
d particle diameter (m)	0.0018	0.0018	0.0018
e_p particle–particle coefficient of restitution	0.95	0.95	0.95

TABLE 1. Parameter values used in the simulation.

4. Symmetric density wave type 1 (SDW1)

When $(\bar{\nu}, \Delta/d) = (0.40, 33.3)$, it is found that the eigenfunction has a symmetric pattern in the density field with two alternating clusters and voids aligning with the centreline (figure 3*a*). Wang *et al.* (1997) identified this mode as SDW1. The base-state solutions for u_0, v_0 and T_0 are not uniform in the transverse direction. These exhibit almost a parabolic distribution with either a concave or convex shape. Hence, it is not easy to visualize the fluctuation of the density field directly. The base-state solutions for the adiabatic wall boundary condition are shown in figure 2 (Wang 1995).

The spatial distributions of ν and ν' values for the temporal evolution of SDW1 mode are shown in figure 3. At $\tau = 0^+$, a small increment in the SDW1 mode eigenfunction (figure 3*a*) perturbs the base state. It is obvious that there are two alternating symmetric clusters or voids of particles aligning beside the centreline. The dense branches are located roughly at $\pm 25\%$ of the channel width away from the centreline. In the subsequent stages of transient integration, the amplitude of ν' continues to increase, as shown in figure 3(*b*). When τ reaches 3.0, the voids begin to split into two or more segments in the flow direction. This amplitude is further enhanced in the later stages at $\tau = 7.2$, as shown in figure 3(*c*). At the same time, the density fluctuations in the particle clusters are amplified till $\tau = 7.2$, where the integration is terminated. Since the highest initial solid fraction is about 0.62, the entire evolution of the SDW1 mode does not take a long time.

The above-mentioned perturbations are superimposed on the base state (uniform in the x-direction; non-uniform in the y-direction) for the purpose of better illustration of the density field. These are displayed in figure 3(*d–i*). With the increment of time from $\tau = 0^+$ to 3.0 (figures 3*d* to 3*f*), the density field becomes much more complicated with a non-uniform periodic structure in the flow direction. When $\tau = 4.5$ (figure 3*g*) the density field starts to develop in a different fashion. The original continuous concentrated regions begin to split (figures 3*h* and 3*i*). As a result, the density field becomes more and more discrete in the flow direction and in certain regions the concentrated clusters are stretched towards the bounding plates. This trend continues till the end of transient integration ($\tau = 7.2$) where the value of ν in certain regions eventually reaches $\nu_m(0.65)$. In this regime, the contribution of friction becomes much more important than collision and hence the basic assumption used in the present study (collision model) fails and no further meaningful conclusions can be drawn.

The interaction between ν and $\boldsymbol{v}$ can be investigated by showing both fields on the same plot as in figures 4(*a*) and 4(*b*) for $\tau = 0^+$ and 7.2, respectively. At $\tau = 0^+$, both density and velocity fields do not deviate much from the base state. When $\tau = 7.2$, the deviation of velocity from a uni-directional flow field becomes more significant. The

https://doi.org/10.1017/S0022112001003792 Published online by Cambridge University Press

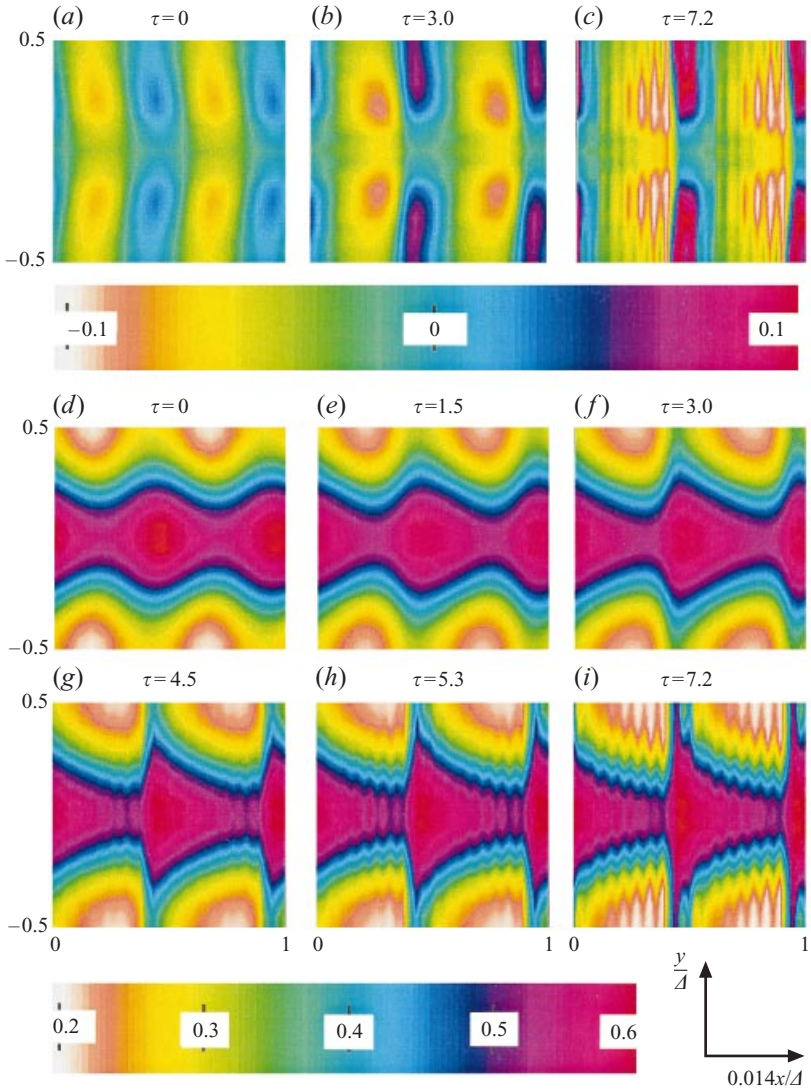


FIGURE 3. Temporal evolution for the SDW1 mode: v' at (*a*) $\tau = 0^+$, (*b*) $\tau = 3.0$, (*c*) $\tau = 7.2$; and v at (*d*) $\tau = 0$, (*e*) $\tau = 1.5$, (*f*) $\tau = 3.0$, (*g*) $\tau = 4.5$, (*h*) $\tau = 5.3$ and (*i*) $\tau = 7.2$.

particles around the dense regions have a tendency to drift towards the two bounding plates.

The FFT analysis is also useful to examine the SDW1 mode in order to get a quantitative understanding of the transient flow. The surface plots of the power spectrum density, P, of v' for the SDW1 mode with the sequence of time are shown in figure 5(*a–f*). When $\tau = 0^+$ (figure 5*a*), there is only one dominant peak existing in the wavenumber domain, which is labelled peak A. It has a preferred x-wavenumber of $f_x = 1$ and y-wavenumber of $f_y = 0$. The x-wavenumber $f_x = 1$ because the computational length in the flow direction just covers one period of the density wave. On the other hand, the dominant peak has a y-wavenumber of $f_y = 0$ which indicates that the periodicity attributed in the transverse direction is quite minor in comparison with that in the flow direction. Due to the view angle, the peak A seems to appear

https://doi.org/10.1017/S0022112001003792 Published online by Cambridge University Press

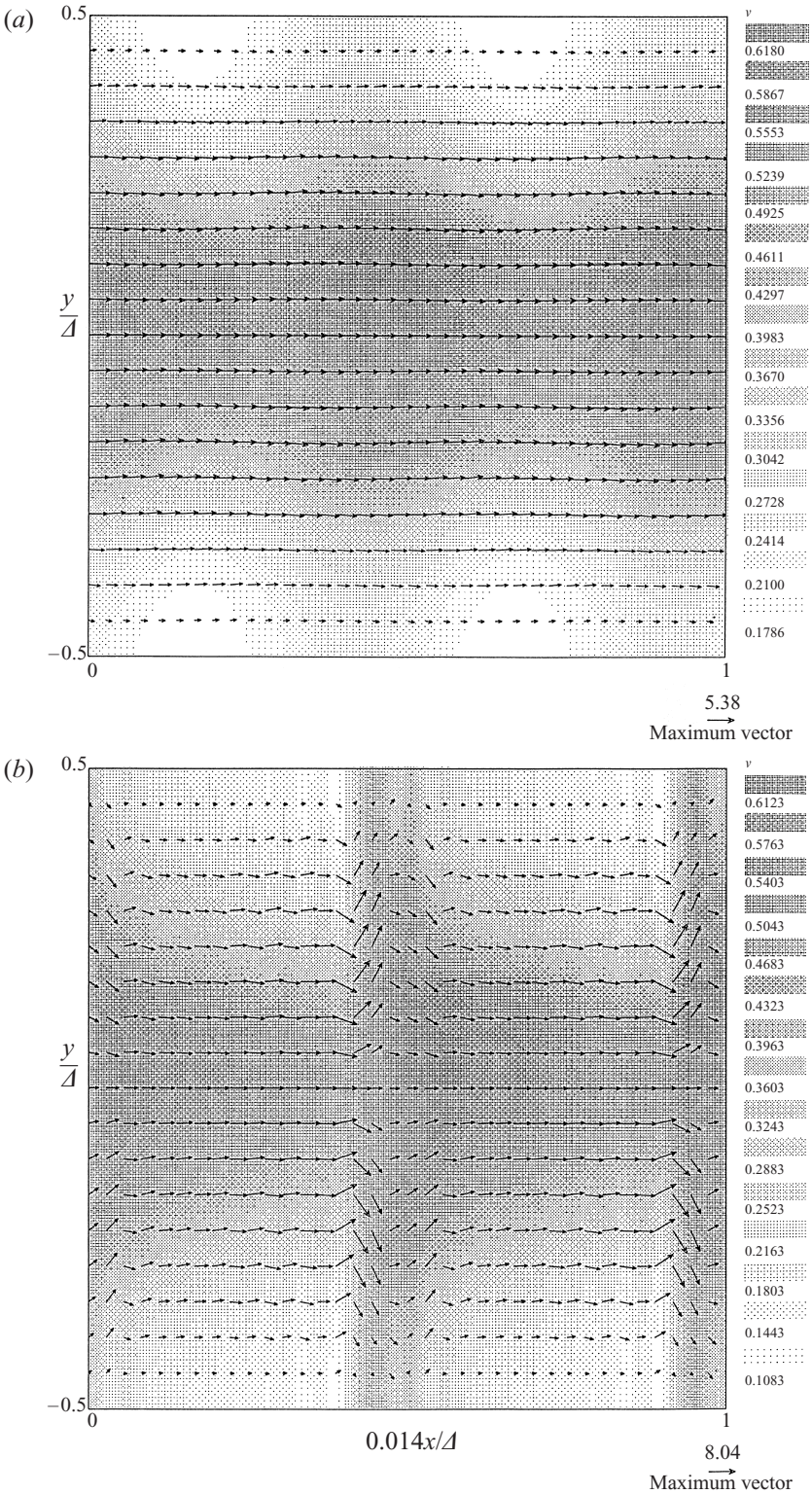


FIGURE 4. Vector plots of $\boldsymbol{v}$ for the SDW1 mode, with shading showing v: (*a*) $\tau = 0^+$ and (*b*) $\tau = 7.2$.

https://doi.org/10.1017/S0022112001003792 Published online by Cambridge University Press

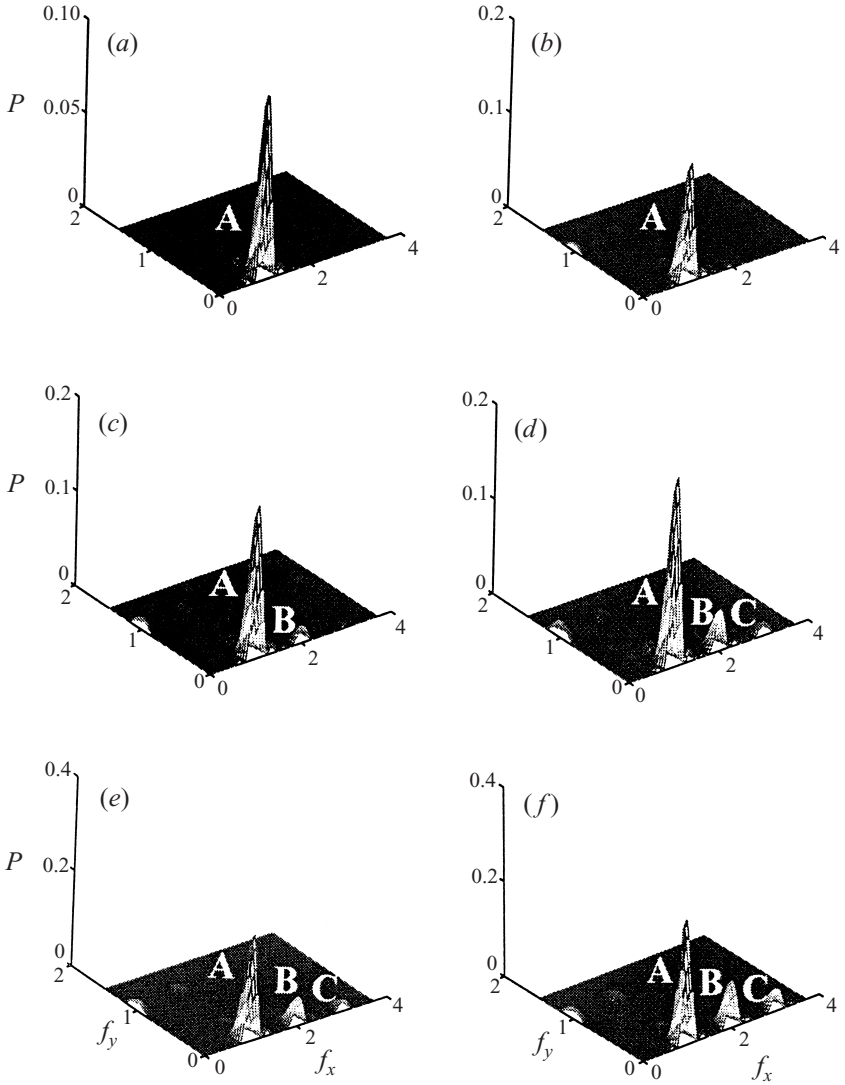


FIGURE 5. Surface plots of the power spectrum density, P, for the SDW1 mode: (*a*) $\tau = 0^+$, (*b*) $\tau = 1.5$, (*c*) $\tau = 3.0$, (*d*) $\tau = 4.5$, (*e*) $\tau = 5.3$ (*f*) $\tau = 7.2$.

at a small positive number on the surface plot. This is because only half of the dominant peak is shown, owing to the symmetry around $f_y = 0$. From $\tau = 0^+$ to 3.0 (figures 5*a* to 5*c*), there is no significant change in the wavenumber domain except the increase of P for peak A. Concurrently, there are a few other smaller peaks scattered around the plot. At $\tau = 3.0$ (figure 5*c*), a new phenomenon can be seen. Another peak labelled B appears with an x-wavenumber of 2 and with a y-wavenumber of 0. This corresponds to the time when the smooth density wave begins to split in the flow direction (figure 3*f*). With further increment in time, peak B becomes more and more significant. At $\tau = 4.5$ (figure 5*d*), one more peak appears at the location (3, 0). This is labelled peak C. These three preferred peaks co-exist and amplify with increasing time in the underlying mean flow. The dominant peak A amplifies throughout the transient integration, indicating that the density field is moving further away from the base state.

https://doi.org/10.1017/S0022112001003792 Published online by Cambridge University Press

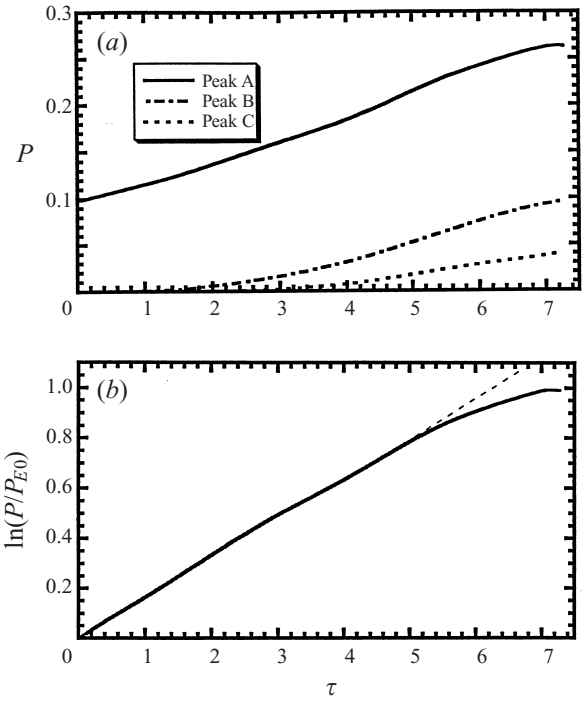


FIGURE 6. Temporal growth of the peaks A, B and C: (*a*) Power spectrum density, P, (*b*) evolution of the SDW1 mode: plot of $\ln(P/P_{E0})$ against τ for the most dominant peak.

As shown in figures 3 and 5, the patterns developed are harmonic distortions of the main waveform ($f_x = 1$). The choice of the smaller x-scale relative to the y-scale in figure 3 is to show the fine structure of the density wave which would not be visible if the x- and y-scales were chosen to be the same. Higher wavenumber modes ($f_x = 2$ and 3) can be captured by figure 5 in which the power of higher harmonic modes is shown. Only the regime $0 < f_x < 4$ is shown because the power of the higher wavenumber modes is much weaker than the first few harmonic modes.

The power spectrum density, P, for the three peaks A, B and C is shown in figure 6(*a*). It is clear from this figure that the peak A dominates throughout the computation, peak B appears in a subsequent stage and peak C appears last. These peaks amplify with time, which makes both the spectral attributes and the spatial distribution of the density wave more and more complicated. Peak A grows in accordance with the linear stability theory except at the end of transient integration. The growth rates of B and C are several orders higher than that of A, resulting in the density wave splitting in the later stages. Since A is the most dominant peak throughout the computation, attention has been paid to understand its development. Figure 6(*b*) shows $\ln(P/P_{E0})$ plotted against τ (P_{E0} refers to the P value of the dominant mode at $\tau = 0^+$). It is seen that the slope generally remains constant except near the end of transient integration, thus indicating that the development of the SDW1 mode is primarily governed by the linear instability.

The initial growth rate and the phase velocity of the SDW1 mode have been compared using FFT, eigenvalue and TNEK (Time-dependent Nekton Viewer) analyses. The corresponding characteristic values are summarized in table 2. From the table, it can be noted that the Ω_r value obtained from FFT analysis is very close to that

https://doi.org/10.1017/S0022112001003792 Published online by Cambridge University Press

Method	Growth rate (Ω_r)	Phase velocity ($-\Omega_i/K_x$)
Eigenvalue analysis	0.076	1.579
Power spectra	0.078	
TNEK		1.391

TABLE 2. Initial characteristic values of the SDW1 mode.

of eigenvalue analysis. The phase velocities predicted from the eigenvalue analysis by Wang (1995) and from the present study are 1.287 and 1.579, respectively. This is cross-checked by TNEK analysis (Lunt 1992), from which the SDW1 mode is found to travel with an initial phase velocity of 1.391 in the flow direction.

5. Symmetric density wave type 2 (SDW2)

At $(\bar{v}, \Delta/d) = (0.15, 33.3)$, the dominant eigenfunction has a symmetric pattern in the density field with a single alternating cluster and void (transverse direction) aligning exactly along the centreline of the channel, and is therefore referred to as the symmetric density wave type 2 (SDW2, figure 7*a*), as reported in Wang *et al.* (1997). The base-state solutions for the adiabatic wall condition are similar to the case of $(\bar{v}, \Delta/d) = (0.15, 33.3)$ shown in figure 2.

In order to investigate the temporal evolution of the density perturbation, the spatial distribution of v with time is shown in figure 7(*a–g*). Two computational cells in the x-direction are shown to elucidate the periodicity in the flow direction. The level of solid concentration can be identified with the change in the colour. Figures 7(*a*)–7(*c*) show the plots of v', while the plots of v are shown in figures 7(*d*)–7(*g*). When $\tau = 0^+$, a small increment in the SDW2 mode perturbation (figure 7*a*) causes non-uniformity in the flow direction (figure 7*d*). This is shown by alternating dense clusters and voids aligning along the centreline. The density wave is symmetric about the centreline, in accordance with the symmetric eigenfunction. When $\tau = 53$ (figure 7*e*), the shape of the density wave changes significantly. The dense regions and void branches have expanded towards the two bounding plates and in the flow direction, respectively.

With the further increase of time beyond $\tau = 227$, a new phenomenon starts to develop as shown in figures 7(*f*) and 7(*g*). The void branches begin to split in the flow direction. The original smooth surface changes into a new terrace-like one. This trend is continued in the subsequent time steps. After stepping into a period of stagnation, v' starts to reshuffle and amplifies rapidly again. At $\tau = 378$ (figure 7*g*), the discrete dense clusters and voids are developed in the flow direction while all regions are divided into small segments. This trend holds in the subsequent stages until the end of the transient integration at $\tau = 801$, where some densely packed clusters are formed (solid fraction = 0.65). The transient integration is terminated there, because the physical limit of the model's assumption has been reached and hence no further conclusions should be drawn. Figures 8(*a*) and 8(*b*) illustrate the interaction of the velocity and density fields at $\tau = 0^+$ and 378, respectively. At $\tau = 0^+$ (figure 8*a*), the velocity field does not deviate much from the base state; on the other hand, at $\tau = 378$ (figure 8*b*), the particles around the dense regions show more obvious lateral movement towards the two bounding plates.

One interesting new finding for the SDW2 mode is the splitting of large particle clusters into smaller ones during the transient development of the flow field. In order to

https://doi.org/10.1017/S0022112001003792 Published online by Cambridge University Press

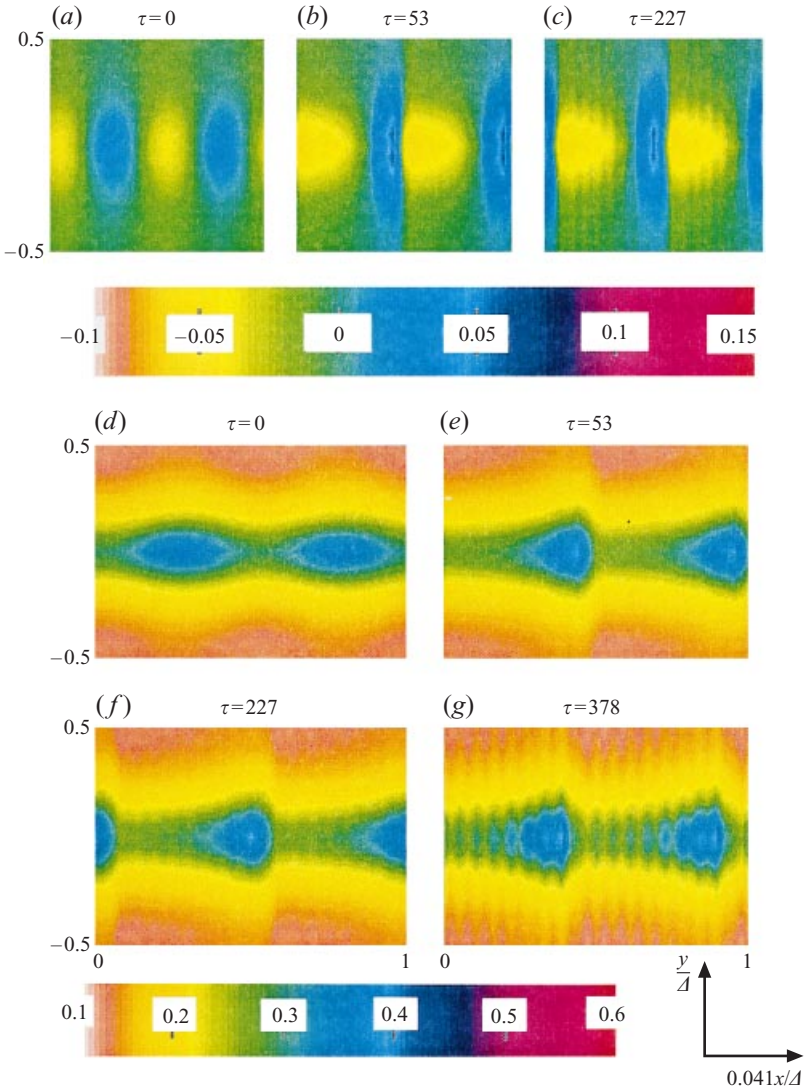


FIGURE 7. Temporal evolution for the SDW2 mode: v' at (*a*) $\tau = 0^+$, (*b*) $\tau = 53$, (*c*) $\tau = 227$; and v at (*d*) $\tau = 0^+$, (*e*) $\tau = 53$, (*f*) $\tau = 227$ and (*g*) $\tau = 378$.

quantify this phenomenon, the fast Fourier transform (FFT) is used. The surface plots of the power spectrum density, P, of v' at a sequence of times are shown in figure 9. When $\tau = 0^+$ (figure 9*a*), there are two peaks existing in the wavenumber domain. The dominant peak (labelled A) has a wavenumber coordinate of $(f_x, f_y) = (1, 0)$, whilst the other peak is labelled B, with a coordinate of (1, 1). It is understandable that both peaks have an x-wavenumber of 1 because the length of the computational cell just covers one period of the density wave in the flow direction. The y-wavenumbers for the peaks are determined by the intrinsic transverse structure of the density wave. It is obvious that peak B is much weaker than peak A in magnitude, which shows that the periodicity of the density wave in the transverse direction is much weaker than the one in the flow direction. By $\tau = 53$ (figure 9*b*), another peak appears at (2, 0), and is labelled C. This implies that the original periodic wave is evolving

https://doi.org/10.1017/S0022112001003792 Published online by Cambridge University Press

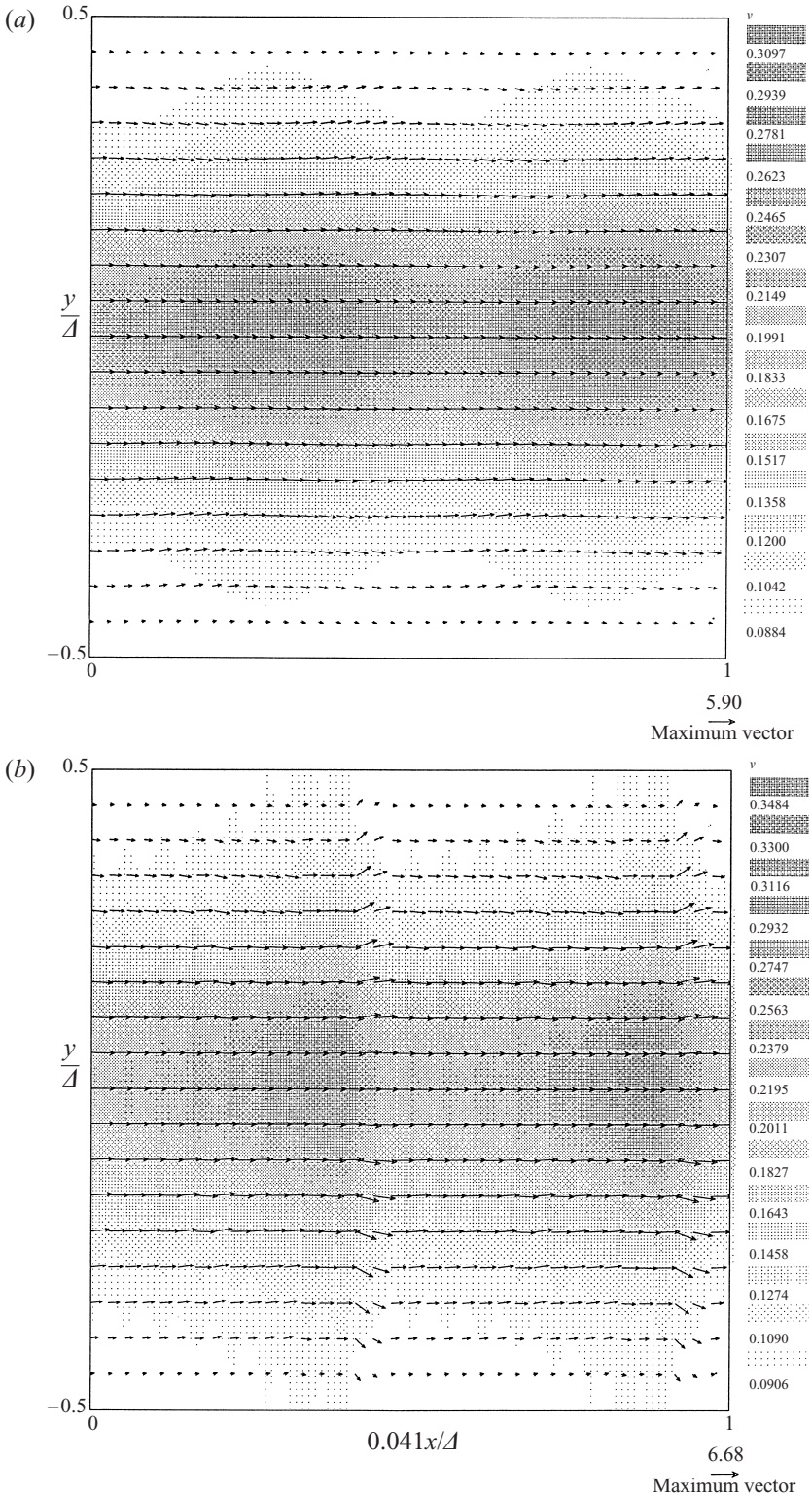


FIGURE 8. Vector plots of $\boldsymbol{v}$ for the SDW2 mode, with shading showing v: (*a*) $\tau = 0^+$ and (*b*) $\tau = 378$.

https://doi.org/10.1017/S0022112001003792 Published online by Cambridge University Press

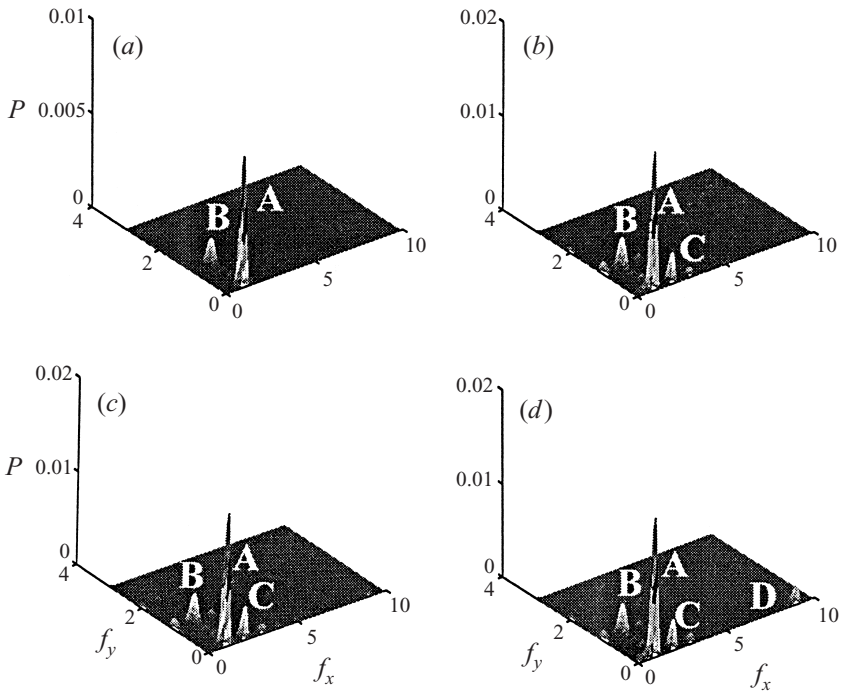


FIGURE 9. Surface plots of the power spectrum density, P, for the SDW2 mode: (*a*) $\tau = 0^+$, (*b*) $\tau = 53$, (*c*) $\tau = 227$ and (*d*) $\tau = 302$.

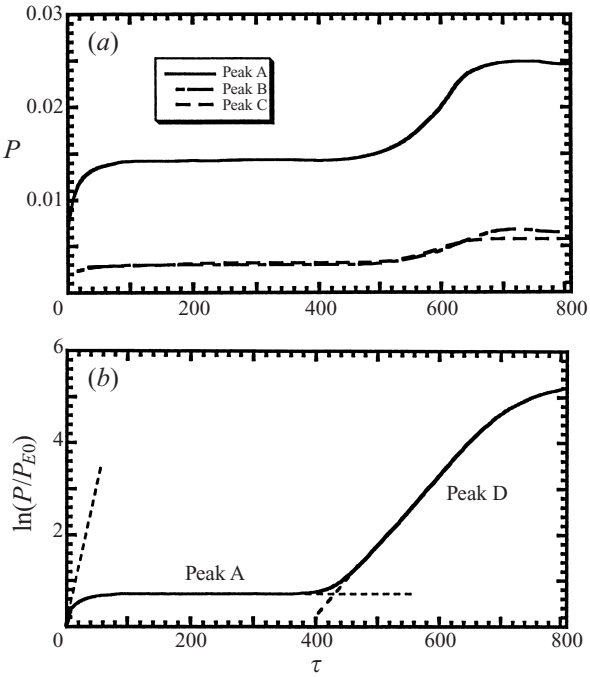


FIGURE 10. Temporal growth of the preferred peaks for the SDW2 mode: (*a*) P for peaks A, B and C, (*b*) evolution of SDW2 mode: plot of $\ln(P/P_{E0})$ against τ for the most dominant peak.

https://doi.org/10.1017/S0022112001003792 Published online by Cambridge University Press

Method	Growth rate (Ω_r)	Phase velocity ($-\Omega_i/K_x$)
Eigenvalue analysis	0.092	6.495
Power spectra	0.092	
TNEK		7.273

TABLE 3. Initial characteristic values of the SDW2 mode.

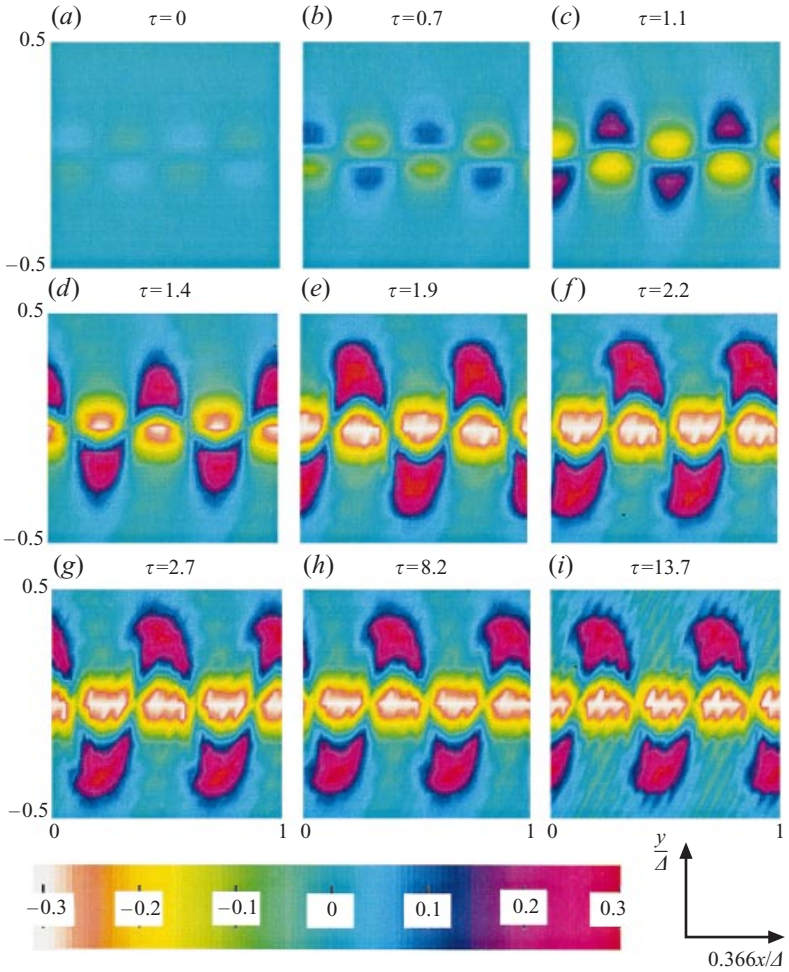


FIGURE 11. Spatial distribution of v' for the ASDW mode: (*a*) $\tau = 0^+$, (*b*) $\tau = 0.7$, (*c*) $\tau = 1.1$, (*d*) $\tau = 1.4$, (*e*) $\tau = 1.9$, (*f*) $\tau = 2.2$, (*g*) $\tau = 2.7$, (*h*) $\tau = 8.2$ and (*i*) $\tau = 13.7$.

into a combination of two harmonic waves in the flow direction. The characteristic feature of the density wave does not change much from $\tau = 53$ to 227 (figures 9*b* to 9*c*), showing that the density wave reaches a stage of retarded growth as explained earlier. At $\tau = 302$ (figure 9*d*), a new peak *D* (location (9, 0)) is greatly amplified. This seems to correspond very well with the fact that the large particle clusters gradually degenerate into nine smaller ones in the flow direction, due to the nonlinearity of the governing equations.

https://doi.org/10.1017/S0022112001003792 Published online by Cambridge University Press

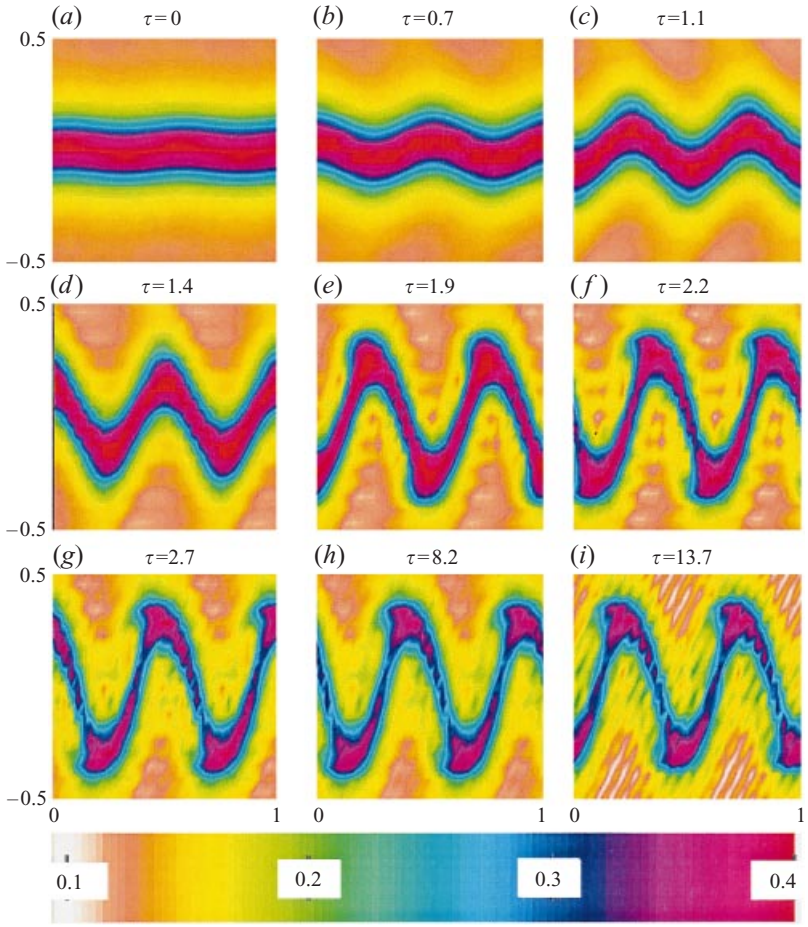


FIGURE 12. Spatial distribution of v for the ASDW mode: (*a*) $\tau = 0^+$, (*b*) $\tau = 0.7$, (*c*) $\tau = 1.1$, (*d*) $\tau = 1.4$, (*e*) $\tau = 1.9$, (*f*) $\tau = 2.2$, (*g*) $\tau = 2.7$, (*h*) $\tau = 8.2$, and (*i*) $\tau = 13.7$.

The evolution of peaks A, B, C and D is investigated in order to get a quantitative understanding of the temporal development of the SDW2 mode. The power spectrum density, P, for A, B and C is shown in figure 10(*a*). It is observed that the P value of peak A increases rapidly at the beginning and then moves into a phase of retarded growth till $\tau = 480$. After that, A has another period of abrupt amplification in the strength of power spectra till $\tau = 620$. Compared with the P value of A, both B and C are minor and do not amplify much after the onset of perturbation.

The envelope of $\ln(P/P_{E0})$ of the most dominant peak against τ is shown in figure 10(*b*). The asymptote branches in the curve actually correspond to the peaks A and D, respectively. The initial behaviour of the density wave is represented primarily by A. The density wave mainly keeps one periodic wave in the flow direction during this period. Peak D grows rapidly at about $\tau = 430$. At later stages, the power spectra of D have a dominant value, several orders of magnitude higher than A. In figure 10(*b*), the overtaking of peak A by peak D is illustrated. In the density plot, this corresponds to the degeneration of large particle clusters into a series of smaller ones.

In summary, the temporal development of the SDW2 mode could be classified

https://doi.org/10.1017/S0022112001003792 Published online by Cambridge University Press

into the following stages: developing with the linear instability in the initial period; then moving into a stage of retarded growth; and finally embarking on the second phase of rapid growth till the end of integration. After the detailed discussion on the temporal evolution of the SDW2 mode, more insight is given to the two characteristic values, Ω_r and $-\Omega_i/K_x$, calculated by FFT, eigenvalue and TNEK analyses. It is seen from table 3 that the measured value of Ω_r from FFT analysis is very close to the corresponding value by eigenvalue analysis. The dimensionless phase velocities predicted by Wang (1995) and the present study are 6.471 and 6.495, respectively. These also agree reasonably well with the TNEK visualization results showing that the SDW2 mode has a phase velocity of 7.273 in the initial period. After the overtaking of peak A by peak D, the phase velocity varies slightly throughout the transient integration.

6. Anti-symmetric density wave (ASDW)

At $(\bar{v}, \Delta/d)$=(0.15, 66.6), it is found that the eigenfunction has another type of pattern in the density field with two anti-symmetric alternating particle clusters and voids aligning beside the centreline. Wang *et al.* (1997) referred this mode as ASDW. The base-state solutions for u_0, v_0 and T_0 are shown in figures 2(*a*), 2(*b*) and 2(*c*), respectively.

In the present investigation the temporal evolution of v' for the ASDW mode is studied. The spatial distribution of v' at selected time steps is shown in figures 11(*a*) to 11(*i*). In the initial period, v' shows a uniform blue colour in most of the flow field except for two small anti-symmetric alternating clusters, as shown in figure 11(*a*). It is found that for the ASDW mode v' is initiated around the centreline of the channel. As shown in figures 11(*b*) to 11(*d*), v' amplifies rapidly with time from $\tau = 0.7$ to $\tau = 1.4$. The particle clusters and voids are greatly intensified in magnitude and expanded. The anti-symmetric pattern develops in such a way that the void regions shift towards the centreline whilst the dense clusters move towards the two bounding plates. As a result, v' changes to another new pattern with a line of void regions along the centreline, accompanied by two lines of alternating dense clusters (figure 11*e*). In the subsequent stages of computation, v' does not change much either in pattern or intensity as shown in figures 11(*f*) to 11(*i*) (from $\tau = 2.2$ to 13.7). However, the flow continues with further redistribution of particles, although the slow evolution is evident.

The spatial distribution of the density wave for the ASDW mode is shown in figures 12(*a*) to 12(*i*). When $\tau = 0^+$ (figure 12*a*), the density wave does not deviate much from the base state. From $\tau = 0.7$ to 1.9 (figures 12*b* to 12*e*), the density pattern changes significantly. The dense stripes at the centreline changed from relatively straight lines into a 'Z' shape. In the subsequent stages till the end, the ASDW mode steps towards the phase of retarded growth as no further significant changes occur in figures 12(*f*) to 12(*i*). The tracking of temporal evolution of the ASDW mode is terminated while some void regions remain empty.

The interaction between the velocity and density fields is investigated by superimposing them on the same plot as shown in figures 13(*a*) and 13(*b*) for $\tau = 0^+$ and 13.7, respectively. As expected, when $\tau = 0^+$, $\boldsymbol{v}$ does not deviate from the base state (one-dimensional flow). When $\tau = 1.9$ (data not shown), the deviation from the uni-directional flow field becomes quite significant and this results in a 'Z'-shaped stream in the flow direction. This phenomenon is further enhanced in subsequent stages as shown in figure 13(*b*) for $\tau = 13.7$.

https://doi.org/10.1017/S0022112001003792 Published online by Cambridge University Press

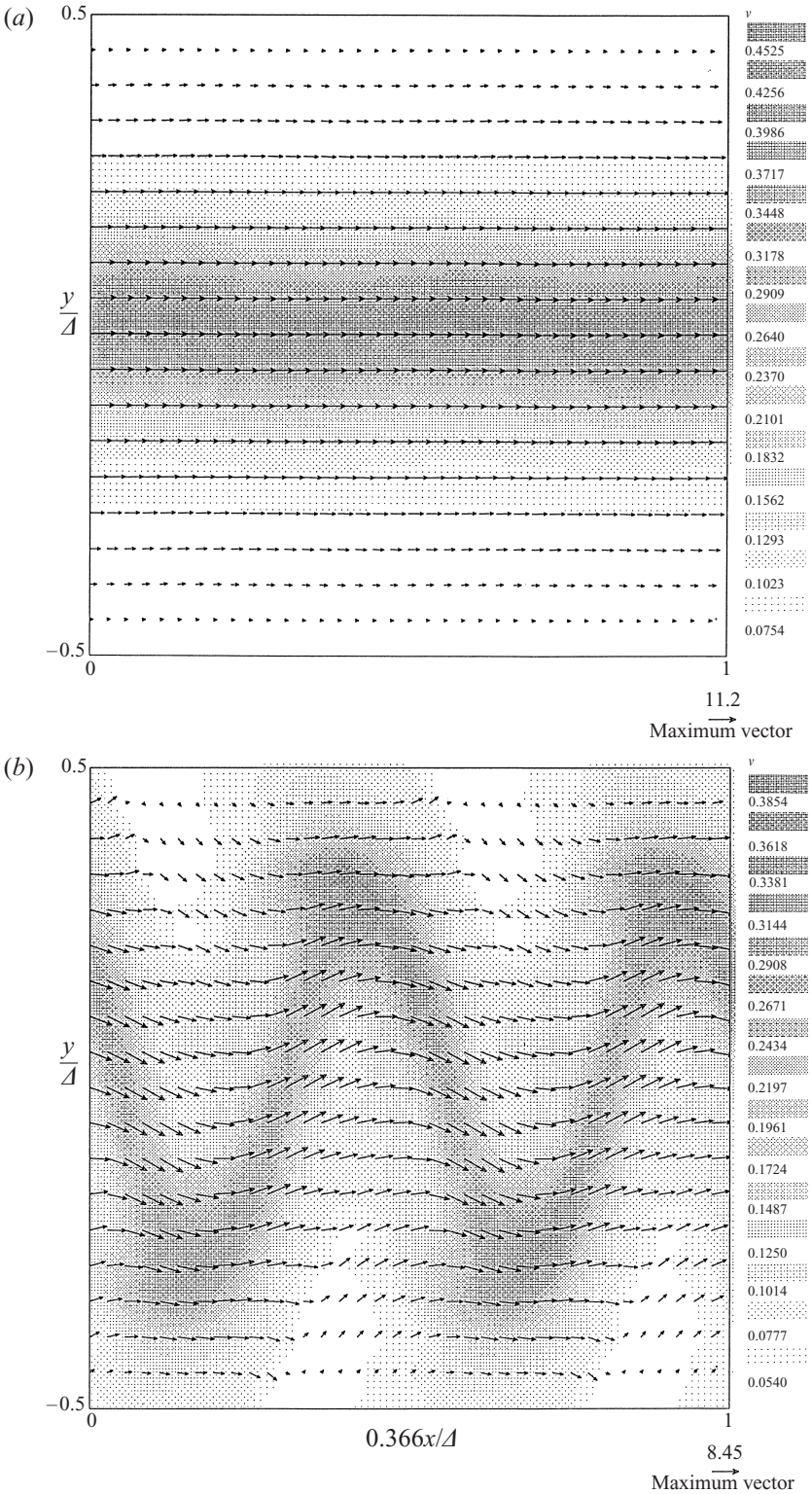


FIGURE 13. Vector plots of $\boldsymbol{v}$ for the ASDW mode, with shading showing v: (*a*) $\tau = 0^+$ and (*b*) $\tau = 13.7$.

https://doi.org/10.1017/S0022112001003792 Published online by Cambridge University Press

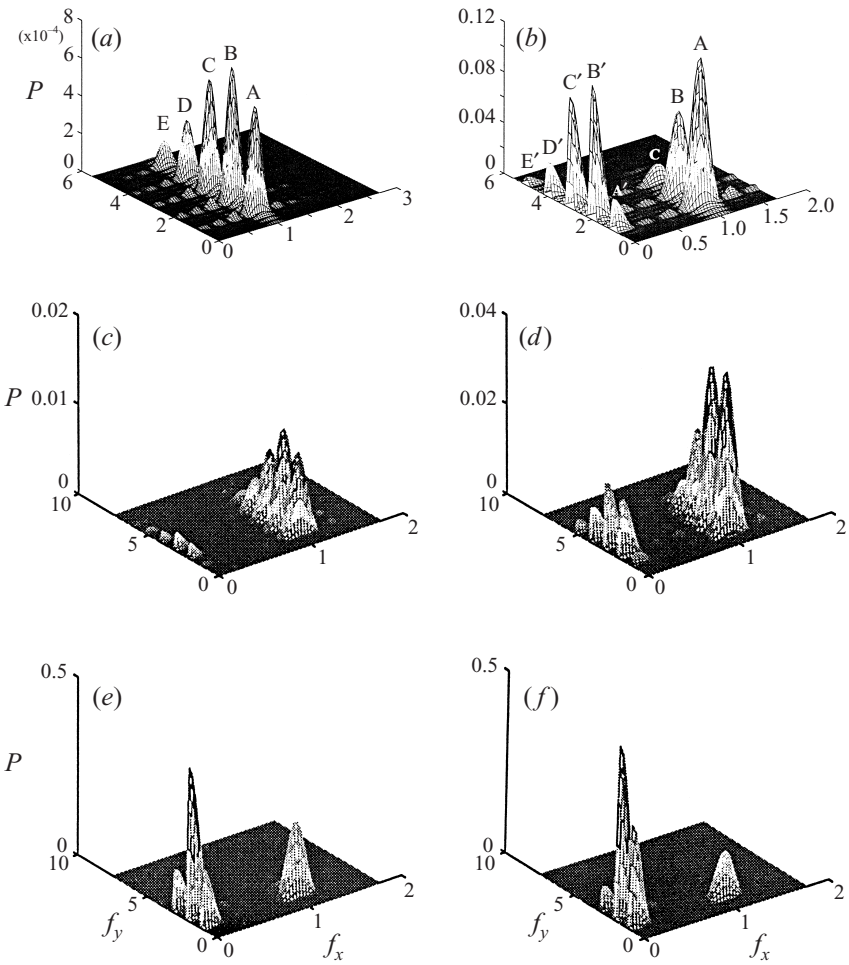


FIGURE 14. Surface plots of the power spectrum density, P, for the ASDW mode: (*a*) $\tau = 0^+$, (*b*) $\tau = 1.4$, (*c*) $\tau = 0.7$, (*d*) $\tau = 1.1$, (*e*) $\tau = 1.9$ and (*f*) $\tau = 13.7$.

The FFT analysis is also carried out to examine the ASDW mode. The surface plots of power spectrum density, P, at a sequence of times are shown in figure 14. When $\tau = 0^+$, all the preferred spectral peaks appear at $f_x = 1$ because of the periodicity in the x-direction. The computational length in the flow direction is chosen just to cover one period of the ASDW mode. These peaks (labelled A, B, C, D and E) have the characteristic y-wavenumbers shown in figure 14(*a*). It is found that peaks A, B, C, D and E have the preferred y-wavenumbers 1, 2, 3, 4 and 5, respectively, indicating that v' is a combination of five major harmonic modes in the transverse direction. This unique spectral attribute distinguishes the ASDW mode from those of the SDW1 and SDW2 modes. In other words, the ASDW mode disturbs the granular flow primarily in the transverse direction rather than in the flow direction, which is characterized by the 'Z'-shaped dense stripes in the density field as discussed earlier. The amplitudes of the peaks A, B, C, D and E amplify rapidly with time. At $\tau = 0.7$ (figure 14*c*), a new series of preferred peaks appears at the x-wavenumber of 0. This newly developed series is comparable in magnitude with the original series, when $\tau = 1.4$ (figure 14*b*). This figure provides clear visualization of the new series of peaks in the wavenumber

https://doi.org/10.1017/S0022112001003792 Published online by Cambridge University Press

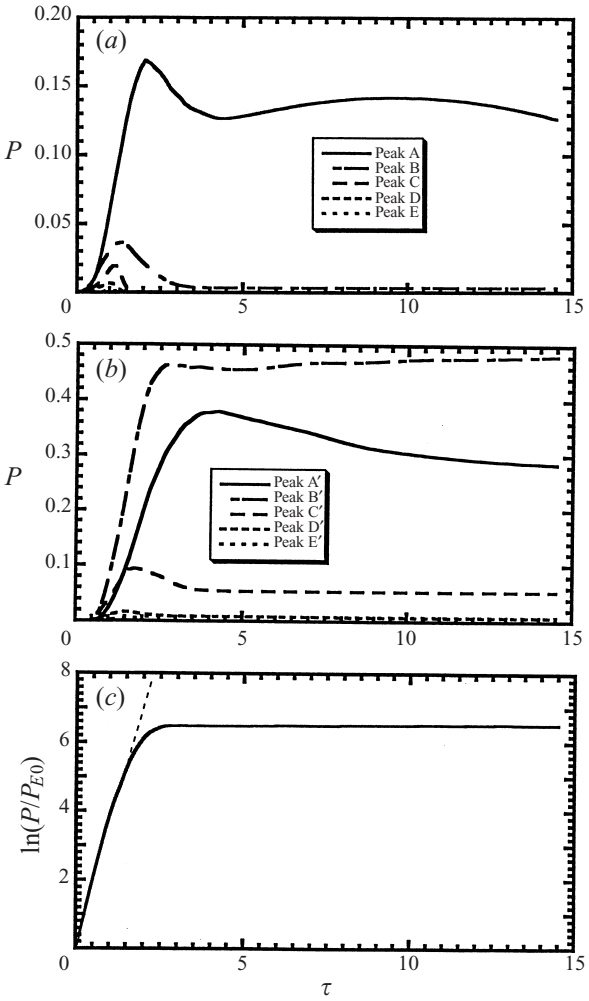


FIGURE 15. Temporal growth of the preferred peaks for the ASDW mode: (*a*) peaks A, B, C, D and E; (*b*) peaks A′, B′, C′, D′ and E′; (*c*) evolution of the ASDW mode: plot of $\ln(P/P_{E0})$ against τ for the most dominant peak.

domain. There are also five peaks aligning at x-wavenumber $= 0$ with characteristic y-wavenumbers of 1, 2, 3, 4 and 5, respectively. They are correspondingly labelled A′, B′, C′, D′ and E′. With the further increment of time (figures 14*e* to 14*f*), the new series of peaks overtakes the original one. This is an important signal showing that the ASDW mode gradually loses its original periodicity in the flow direction.

The evolution of the preferred peaks of the ASDW mode is also investigated in the present study. Figure 15(*a*) shows the temporal evolution of A, B, C, D and E. It is found that they are all amplified in the initial period of the transient integration. At a later stage, only peak A maintains a significant value of P whilst others become minor compared to A. Figure 15(*b*) shows the temporal evolution of the peaks A′, B′, C′, D′ and E′. Apparently A′, B′, C′ rise rapidly in the initial period, and become the most important peaks of the ASDW mode at later stages. The comparison between peaks A and B′ (figures 15*a* and 15*b*), the most dominant peaks of the two series,

https://doi.org/10.1017/S0022112001003792 Published online by Cambridge University Press

Method	Growth rate (Ω_r)	Phase velocity ($-\Omega_i/K_x$)
Eigenvalue analysis	1.860	9.569
Power spectra	1.925	
TNEK		9.693

TABLE 4. Initial characteristic values of the ASDW mode.

shows that peak B′ overtakes peak A at around $\tau = 1.4$. This is a critical point for the ASDW mode as it designates the loss of periodicity in the flow direction.

For the first series, all the five peaks grow rapidly with about the same growth rate. Subsequently, peak A seems to move to a steady state and the others start to decrease drastically. The development of peaks A′, B′, C′, D′ and E′ is also governed by the linear instability in the initial period. From around $\tau = 1.9$ onwards, their development gradually slows down. This is reflected in the temporal evolution of the density field as already discussed whereas its pattern and intensity do not change much from $\tau = 1.9$ to 13.7. The envelope of $\ln(P/P_{E0})$ against τ for the most dominant peak of the ASDW mode is shown in figure 15(*c*). It is seen that the ASDW mode grows rapidly in the initial period, in accordance with the linear stability theory, and later it enters into a relatively slow evolving state until some void regions become empty.

The characteristic values of Ω_r and $-\Omega_i/K_x$ calculated by different methods are tabulated in table 4. It is obvious that Ω_r of the initial period obtained through the power spectrum analysis ($\Omega_r = 1.925$) is again very close to that by the eigenvalue method. The initial phase velocity predicted by the present study ($-\Omega_i/K_x = 9.569$) is quite consistent with that obtained by Wang (1995), $-\Omega_i/K_x = 9.855$. The independent TNEK analysis affirms that the ASDW mode travels with an initial phase velocity of 9.693 in the initial period. With the development of the ASDW mode, the phase velocity gradually slows down to 5.816 before the end of transient integration. In other words, the phase velocity is reduced by 40% during the transient development!

7. Comparison among the SDW1, SDW2 and ASDW modes

The growth rates evaluated through the power spectrum analysis in the initial period for all three modes are compared. It is clear that the SDW1 and SDW2 modes develop with initial growth rate in the order of 0.01 to 0.1, which is more than two orders of magnitude smaller than that of the ASDW mode. The short-term and long-term behaviours of these three modes are also quite different. The SDW2 mode shows a complicated behaviour throughout the period. It first grows in accordance with the linear stability theory and then quickly moves into a phase of retarded growth. When $\tau = 435$, it embarks on the second phase of abrupt growth till the end of computation. In contrast, for the SDW1 mode, the evolution is much more straightforward. The temporal development of the SDW1 mode is primarily governed by the linear instability except near the end of the transient integration. There are two stages of development for the ASDW mode. In the initial period it rises rapidly in accordance with the linear instability, and soon it enters into a stage of retarded growth until some void regions become empty. The long-term behaviours of the phase velocity ($-\Omega_i/K_x$) for the SDW1, SDW2 and ASDW modes are also different. The SDW1 and SDW2 modes maintain their phase velocity within $\pm 10\%$ of the original value throughout the transient integration, in contrast to the ASDW

https://doi.org/10.1017/S0022112001003792 Published online by Cambridge University Press

mode in which the velocity slows down by 40% from the onset of perturbation to the end of integration.

The spectral attributes of v' for the SDW1, SDW2 and ASDW modes are characterized by their own sets of harmonic modes. For the SDW1 and SDW2 modes, v' primarily comprises a series of harmonic modes in the flow direction. In contrast, for the ASDW mode, v' primarily comprises a series of harmonic modes in the transverse direction, indicating that its evolution is governed by transverse development.

8. Mechanism of instabilities

The mechanisms of instabilities are examined by a term-by-term analysis of the governing equations. This is significantly different from the analysis of the physical mechanism of the pattern formation. The latter approach has been extensively reported in the literature, better known as the particle dynamics simulation (Lee 1994; Lee & Leibig 1994; Peng & Herrmann 1994, 1995).

As discussed in the previous sections, a passive (adiabatic) wall may still trigger complicated density waves without the rough-wall condition. When an adiabatic-wall condition is applied, three modes of characteristic density waves exist. This signifies that the wall roughness is not the necessary condition for the emergence of instabilities as long as the particle–particle collisions are inelastic. This appears to be different from the findings of Peng & Herrmann (1994), which showed that both the wall roughness and inter-particle collisions are necessary conditions for triggering density waves in gravity pipe flows of granular materials.

When the walls act as either sink or source of pseudo-thermal energy, the wall may interact with the flow field and thereby modifies the structure of density waves. Two issues remain to be answered in this study. First, the mechanism of the instabilities reported in earlier sections and secondly, the alteration of density wave structure when the boundary condition is changed form an 'adiabatic' to a 'sink wall'. The first point is studied by adding two empirical coefficients α and β to the momentum and energy equations, respectively:

$$\alpha\rho\frac{\mathrm{D}\boldsymbol{u}}{\mathrm{D}t} = -\nabla\cdot\boldsymbol{\sigma} + \rho\boldsymbol{g}, \tag{12a}$$

$$\beta\frac{3}{2}\rho\frac{\mathrm{D}T}{\mathrm{D}t} = -\nabla\cdot\boldsymbol{q} - \boldsymbol{\sigma}{:}\nabla\boldsymbol{u} - J, \tag{12b}$$

where $\rho = \rho_s v$. The parameters α and β are then varied and the real and imaginary parts of the eigenvalue of the dominant mode, Ω, along with its corresponding dimensionless wavenumber, K_x are calculated. The most dominant growth rate and phase velocity for the specified values of α and β can be found from these calculated values. To examine the second point regarding the effect of boundary conditions, the value of parameters used in this section are the same as in table 1 except that a 'sink-wall' boundary condition is used instead ($e_w = 0.5$, $\varphi' = 0.6$).

In order to study the mechanism, the growth rate and the phase velocity are plotted against the parameters α and β, respectively. In addition, to examine the structure of instabilities, the most dominant eigenfunctions of the fluctuations in solid concentration are also shown at specified values of α, known as density plots.

Figure 16(a) shows the dimensionless growth rate, Ω_r, and the phase velocity ($-\Omega_i/K_x$), plotted against α for the SDW2 mode. As the α value decreases from 1 (full inertial effect), the growth rate also decreases. The growth rate changes from

https://doi.org/10.1017/S0022112001003792 Published online by Cambridge University Press

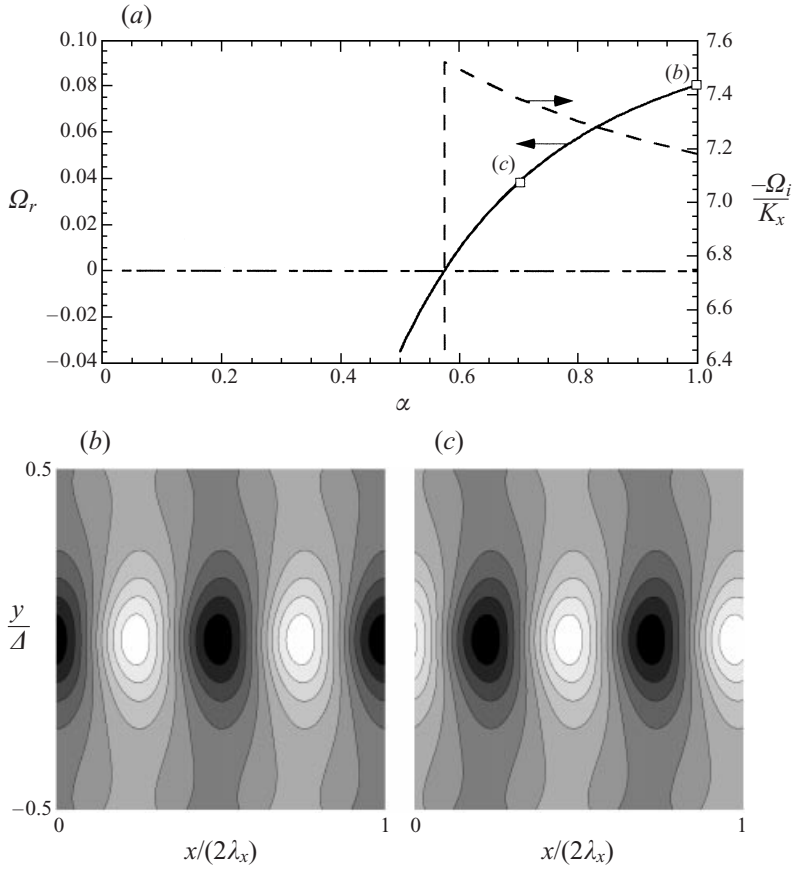


FIGURE 16. Effect of α on the stability of flow for the SDW2 mode at the point $(\bar{\nu}, \Delta/d) = (0.15, 33.3)$, $(e_w, \varphi') = (0.5, 0.6)$. (*a*) Growth rate ($\Omega_r$) and phase velocity ($-\Omega_i/K_x$) vs α. (*b*) Dominant travelling-wave mode eigenfunction at $\alpha = 1.0$, (*c*) $\alpha = 0.7$. The left- and right-hand axes refer to Ω_r and $-\Omega_i/K_x$, respectively.

a positive value to a negative one (that is, the flow becomes stable) if the inertial effect is reduced below 0.6. This mathematical solution seems to support the idea that SDW2 is triggered partially by momentum inertia. The stability characteristics of the flow change at a critical value of $\alpha_{crit} = 0.58$, accompanied by the crossing of one branch to another. Hence, the momentum inertia destabilizes the gravity-driven granular flow. In the phase velocity curve, the velocity increases as α is decreased. Similarly, there is a discontinuity in the phase velocity at $\alpha_{crit} = 0.58$ due to a change in the dominant branch. The value of the phase velocity remains 'positive' indicating that the flow direction of the density wave is the same as the flow of particles.

Figures 16(*b*) and 16(*c*) show the most dominant solid concentration density at $\alpha = 1.0$ and $\alpha = 0.7$ respectively. With reference to the schematic diagram of figure 1, these figures are orientated in such a way that gravity is acting along the x-axis. The darker regions indicate higher solid concentration while the lighter regions indicate lower solid concentration. Figures 16(*b*) and 16(*c*) have a similar pattern (opposite phase, recalling that any constant – either positive or negative – multiple of an eigenfunction is still an eigenfunction of the original physical problem), indicating that points (*b*) and (*c*) in figure 16(*a*) are on the same eigenfunction branch. Similar

https://doi.org/10.1017/S0022112001003792 Published online by Cambridge University Press

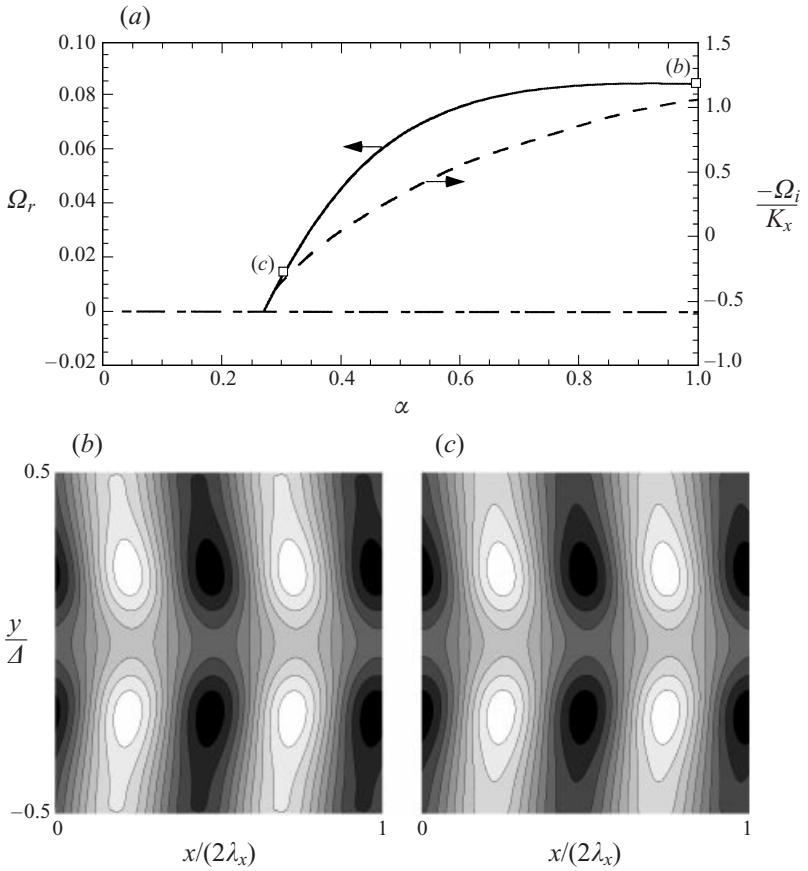


FIGURE 17. Effect of α on the stability of flow for the SDW1 mode at the point $(\bar{\nu}, \Delta/d) = (0.40, 33.3)$, $(e_w, \varphi') = (0.5, 0.6)$. (*a*) Growth rate ($\Omega_r$) and phase velocity ($-\Omega_i/K_x$) vs α. (*b*) Dominant travelling-wave mode eigenfunction at $\alpha = 1.0$, (*c*) $\alpha = 0.3$. The left- and right-hand axes refer to Ω_r and $-\Omega_i/K_x$, respectively.

calculations have been carried out for β and the results show that it has an opposite effect on the momentum inertia. The growth rate increases as β decreases and the mode remains unstable without any changes in the dominant branch. The phase velocity remains positive, but decreases as the value of β decreases (data not shown).

The momentum inertia has a similar effect on the SDW1 mode as shown in figure 17. The growth rate, Ω_r, decreases as α is decreased and a stable mode is attained at $\alpha_{crit} = 0.27$. Similar to the SDW2 mode, a crossing of branches is also observed here. The difference in the effect of α on the SDW1 and SDW2 modes is that in the SDW1 mode, the phase velocity decreases as α decreases and the negative phase velocity is obtained at $\alpha \leqslant 0.4$. Hence, the momentum inertia reduces the stability of the granular flow.

The effects of α on the ASDW mode are also examined. The results shown in figure 18 indicate that the momentum inertia also destabilizes the flow. The crossing of the dominant branches occur at two places. The first crossing is at $\alpha = 0.33$ and the second one is the crossing of an unstable mode to a stable one at $\alpha_{crit} = 0.01$. A similar trend is also observed in the phase velocity curve. Crossings of the dominant branches are observed at $\alpha = 0.33$ and $\alpha_{crit} = 0.01$. The phase velocity of the ASDW

https://doi.org/10.1017/S0022112001003792 Published online by Cambridge University Press

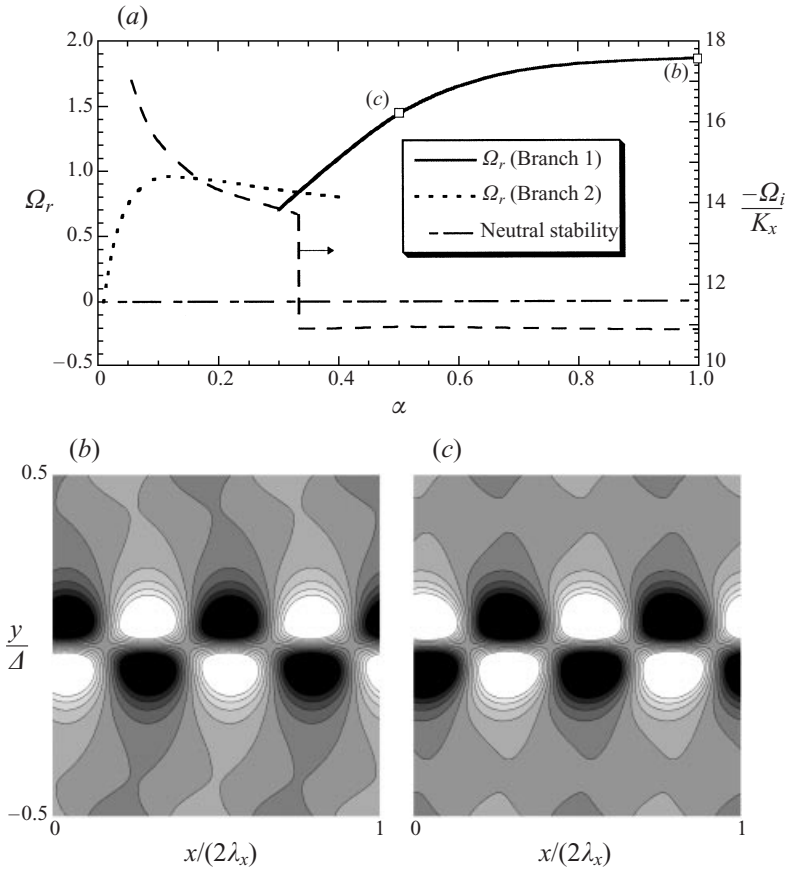


FIGURE 18. Effect of α on the stability of flow for the ASDW mode at the point $(\bar{v}, \Delta/d) = (0.15, 66.6)$, $(e_w, \varphi') = (0.5, 0.6)$. (*a*) Growth rate ($\Omega_r$) and phase velocity ($-\Omega_i/K_x$) vs α. (*b*) Dominant travelling-wave mode eigenfunction at $\alpha = 1.0$, (*c*) $\alpha = 0.5$. A legend is inserted to clarify the line styles associated with the growth rates for the two branches (denoted as branches 1 and 2, respectively, left-hand axis). The phase velocity ($-\Omega_i/K_x$) is the dashed line shown by a right-hand arrow.

mode is found to be greater than that of the SDW modes. The solid concentration distributions in the figures 18(*b*) and 18(*c*) appear slightly different but the basic pattern is similar.

The density eigenfunction comparisons among figures 16(*b*), 17(*b*) and 18(*b*) with those of figures 3(*a*), 7(*a*) and 11(*a*) show that the nature of the dominant modes does not change significantly with the variation of boundary conditions. However, this does not exclude the possibility that the temporal evolution of different modes may be affected by the variation of the wall condition: this problem remained to be investigated in our future studies.

9. Comparison with previous studies

9.1. *Numerical studies*

The theoretical works of Peng & Herrmann (1994, 1995) are largely based on a lattice-gas automata (LGA) model in which probabilistic collision rules for particle collisions are proposed and the resulting particle distributions are tracked. These differ from the

https://doi.org/10.1017/S0022112001003792 Published online by Cambridge University Press

present study in which model continuum constitutive relations for granular materials are employed in the conservation equations of mass, momentum, and energy. Peng & Herrmann (1994, 1995) presented their results in terms of the time evolution of the density field, highlighting the variation along the pipe for various probabilistic collision parameters. At a fixed value of gravitational acceleration, these LGA models predict nearly constant phase velocities for various bed densities. Furthermore, the LGA models do not differentiate between the particle and phase velocities. This seems to be in direct contrast with the findings of the present study in which the phase velocity ($-\Omega_i/K_x$) of the density waves varies significantly with the gap width (Δ/d) and solid fraction (ν). For instance, the phase velocity of the ASDW, (($\Delta/d, \nu$) = (66.6, 0.15)) is nearly six times and 33% larger than the SDW1 mode (($\Delta/d, \nu$) = (33.3, 0.15)) and SDW2 mode (($\Delta/d, \nu$) = (33.3, 0.4)), respectively. While the phase velocity can be different from the average velocity of the granular assembly, its value can also vary with time by more than 40% according to the transient integration results indicated elsewhere in this work.

9.2. *Experimental studies*

Savage (1979) observed a flat particle velocity profile in the centre of a vertical channel and significant shear near the walls. These profiles seem to be similar to the base-state profiles shown in figure 2. The diameter ratio of pipe to particle employed in Nakaharan & Isoda (1997) is in general less than 10, much smaller than the corresponding values in the present work (greater than 33). It is not surprising to see that the flow patterns predicted in the present study have more significant lateral structure than the one-dimensional structure observed in Nakaharan & Isoda (1997). In contrast, the simulations of the present work can be better compared with the complicated two-dimensional density wave observed in Horikawa *et al.* (1996), Aider *et al.* (1999) and Hua & Wang (1999) owing to their much closer pipe/particle diameter ratio (their values are roughly in the range 10–30).

Using a digital charge coupled device camera, Aider *et al.* (1999) observed propagative and oscillating waves in an intermediate mass-flow-rate regime where high-compactness 'clogs' are separated by low-density 'bubbles'. These clogs have a characteristic wavelength in the order of 1 cm, in contrast to the equivalent wavelength of the ASDW (1.6 cm), SDW1 (41 cm) and SDW2 (14 cm) in the present study for similar sizes of pipes and particles, but different particle concentration and flow geometry. Hua & Wang (1999) employed electrical capacitance tomography to investigate the density wave formation for two different types of particles in a vertical pipe. They observed the temporal variation of particle distribution by a series of snapshots taken at a cut section of the pipe. The resulting images illustrate the spatiotemporal variations of the density wave corresponding to the side views of the particle concentration contours shown in figure 3, 7 and 12 of the present work.

10. Conclusions

This paper contains the first integration of a set of continuum equations for a rapid flow of a granular material in both space and time. By comparing the model predictions with previous studies in the literature, the present work also provides an indirect way to examine the validity of the constitutive relations commonly employed in the grain kinetic theory. The findings of this work support the idea that complicated density wave patterns can be caused by the collisions between particles even in the absence of an interstitial fluid.

https://doi.org/10.1017/S0022112001003792 Published online by Cambridge University Press

The initial development of three types of travelling density waves in the gravity-driven, flow, namely SDW1, SDW2 and ASDW modes, is triggered by linear instability. Significant nonlinear development is observed in the ASDW mode at the later stages of the transient integration. FFT and power spectrum analyses are able to capture the temporal evolution of the density waves. The preferred intrinsic modes are filtered out effectively by the FFT analysis and can be used to characterize the gravity-driven flow.

The findings of the present study also indicate that wall roughness may contribute to and modify the patterns but may not be the necessary condition for triggering the density waves in gravity channel flow. All three modes of instabilities reported in this work are of inertial origin and occur when the collisions between particles are inelastic.

This work has been supported by the National University of Singapore (NUS) under the grant number RP960630. C.-H. Wang thanks Professors Roy Jackson and Sankaran Sundaresan of Princeton University for their comments on the project. Both authors would like to thank the Institute of High Performance Computing (Singapore) and Silicon Graphics Inc. for the usage of supercomputing facilities, and Loke Keat Thong for his technical support.

Appendix. Numerical methods used in the eigenvalue and transient analyses

A basic computational unit cell consists of an $m \times m$ grid of rectangular cells. Two consecutive cells are shown in figures 3, 4, 7, 8, 11, 12, and 13 to indicate the periodicity in the x-direction. The finite-element equations of (1) to (3) are

$$\boldsymbol{A} \cdot \dot{\boldsymbol{y}} + \boldsymbol{f}(\boldsymbol{y}) = \boldsymbol{0}, \tag{A 1}$$

$$\boldsymbol{A} = \begin{bmatrix} \boldsymbol{A}_1 & 0 & 0 & 0 \\ 0 & \boldsymbol{A}_2 & 0 & 0 \\ 0 & 0 & \boldsymbol{A}_3 & 0 \\ 0 & 0 & 0 & \boldsymbol{A}_4 \end{bmatrix}, \tag{A 2}$$

$$\boldsymbol{y} = \begin{bmatrix} \boldsymbol{y}_1 \\ \boldsymbol{y}_2 \\ \boldsymbol{y}_3 \\ \boldsymbol{y}_4 \end{bmatrix}, \qquad \boldsymbol{f} = \begin{bmatrix} \boldsymbol{f}_1 \\ \boldsymbol{f}_2 \\ \boldsymbol{f}_3 \\ \boldsymbol{f}_4 \end{bmatrix}, \tag{A 3), (A 4}$$

where $\boldsymbol{A}$ and $\boldsymbol{f}$ with subscripts 1, 2, 3, and 4 refer to the terms of the continuity equation (1), x-momentum equation (2), y-momentum equation (3), and the energy balance equation (4), respectively. The components y_1–y_4 of vector $\boldsymbol{y}$ represents the volume fraction, x- and y-velocity components, and granular temperature, respectively. The expressions for $\boldsymbol{A}$ and $\boldsymbol{f}$ involve a variety of integrals of basis functions and integrals of products of basis function and variables. The basis functions are chosen to be biquadratic functions of the coordinates. The integrals are evaluated by the summation over Gaussian quadrature points (4×4) while the transient values of variables u, v, v and T are evaluated on the regular grid points (3×3) for each mesh. The elements and variables used in this study are:

number of elements $= m^2$,
number of variables for $v = 2m(2m + 1)$,
number of variables for $u(v \text{ or } T) = 2m(2m - 1)$,
total number of variables $(\boldsymbol{y})$: $2m(2m + 1) + 6m(2m - 1)$.

https://doi.org/10.1017/S0022112001003792 Published online by Cambridge University Press

Because the periodicity occurs only in the x-direction, there are $2m$ nodal points in the x-direction while there are $2m+1$ nodal points in the y-direction. The product of these two numbers gives the number of variables for v to be $2m(2m+1)$. The values of u, v, and T on the boundaries located at $Y = \pm 0.5$ are easily written down explicitly in terms of interior variables, leaving fewer unknowns.

In order to examine the stability of a base state, $\boldsymbol{f}(\boldsymbol{y})$ in (A 1) is linearized around its base state $\boldsymbol{y}_0'$.

$$\boldsymbol{f}(\boldsymbol{y}) = \boldsymbol{J}_0(\boldsymbol{y} - \boldsymbol{y}_0), \quad \boldsymbol{f}(\boldsymbol{y}_0) = \boldsymbol{0}, \tag{A 5}$$

where $\boldsymbol{J}_0 = (\partial \boldsymbol{f}/\partial \boldsymbol{y})\boldsymbol{y}_0$ is the numerical Jacobian.

Denoting $\hat{\boldsymbol{y}} \equiv \boldsymbol{y} - \boldsymbol{y}_0$, we have $\dot{\boldsymbol{y}} \equiv \dot{\hat{\boldsymbol{y}}}$ and equation (A 1) becomes

$$\boldsymbol{A}(\boldsymbol{y}_0)\dot{\hat{\boldsymbol{y}}} = -\boldsymbol{J}_0\hat{\boldsymbol{y}}. \tag{A 6}$$

We then consider a perturbation of the following form:

$$\hat{\boldsymbol{y}} = \boldsymbol{\Psi} \mathrm{e}^{\lambda t} \tag{A 7}$$

Substituting equation (A 7) into equation (A 5) and rearranging we obtain

$$\boldsymbol{A}(\boldsymbol{y}_0)\lambda\boldsymbol{\Psi} = -\boldsymbol{J}_0\boldsymbol{\Psi}. \tag{A 8}$$

The generalized eigenvalue problem is solved by LAPACK routine 'rgg'. The eigenvalues and the corresponding eigenvectors are recorded. A small fraction ($< 5\%$) of the least-stable eigenvector is then added to the base-state solution to generate the initial condition for a time-dependent problem of the full nonlinear equation (A 1). The solution is integrated forwarded in the time domain. In order to carry out the numerical integration, equation (A 1) is approximated by

$$\boldsymbol{A}^n \cdot \boldsymbol{y}^{n+1} = \boldsymbol{A}^n \cdot \boldsymbol{y}^n - \Delta t \cdot \boldsymbol{f}(\boldsymbol{y}^n) = \hat{\boldsymbol{f}}(\boldsymbol{y}^n). \tag{A 9}$$

Equation (A 9) has the form $\boldsymbol{A} \cdot \boldsymbol{X} = \boldsymbol{B}[B \Rightarrow \hat{\boldsymbol{f}}(\boldsymbol{y}^n)]$. The superscripts n and $n+1$ denote the time steps at which the numerical integration is carried out. This is solved by LAPACK routines 'dgetrf' and 'dgetrs': 'dgetrf' computes the LU factorization of a general $(16m^2 - 4m) \times (16m^2 - 4m)$ matrix using partial pivoting with row exchange, while 'dgetrs' solves a system of linear equations using the LU factorization computed from 'dgetrf'.

The spatial and temporal resolution has been examined by varying the time step and grid size respectively to ensure the convergence falling within $\pm 0.01\%$. The finite-element formulation involves a rectangular grid mesh solved by various standard mathematical software packages. Taking the mesh refinement test of the ASDW (anti-symmetric density wave) mode as an example, we have examined the 25×25 mesh points (with a 2256×2256 matrix equation) and 19×19 mesh points (with a 1260×1260 matrix equation) in a computational unit cell (the domain displayed in figure 12 covers two unit cells in the x-direction). Furthermore, the time steps ($\Delta\tau$) of 0.000125 and 0.00025 have been verified, subjected to the same criterion indicated above.

REFERENCES

AIDER, J.-L., SOMMIER, N., RAAFAT, T. & HULIN, J.-P. 1999 Experimental study of a granular flow in a vertical pipe: A spatiotemporal analysis. *Phys. Rev.* E **59**, 778–786.

ASTARITA, G. & OCONE, R. 1994 Large-scale statistical thermodynamics and wave-propagation in granular flow. *Ind. Engng Chem. Res.* **33**, 2280–2287.

https://doi.org/10.1017/S0022112001003792 Published online by Cambridge University Press

Babić, M. 1993 Gravity-driven flows of smooth, inelastic disks between parallel bumpy boundaries. *J. Appl. Mech.* **60**, 59–64.

Bagnold, R. A. 1954 Experiments on a gravity-free dispersion of large solid spheres in Newtonian fluid under shear. *Proc. R. Soc. Lond.* A **225**, 49–63.

Bolio, E. J. & Sinclair, J. L. 1995 Gas turbulence modulation in the pneumatic conveying of massive particles in vertical tubes. *Intl J. Multiphase Flow* **21**, 985–1001.

Dudgeon, D. E. & Mersereau, R. M. 1984 *Multidimensional Digital Signal Processing*. Prentice-Hall.

Goodman, M. A. & Cowin, S. C. 1971 Two problems in gravity flow of granular materials. *J. Fluid Mech.* **45**, 321–339.

Horikawa, S., Isoda, T., Nakayama, T., Nakahara, A. & Matsushita, M. 1996 Self-organized critical density waves of granular particles flowing through a pipe. *Physica* A **233**, 699–708.

Hua, J. & Wang, C.-H. 1999 Electrical capacitance tomography measurements of gravity-driven granular flows. *Ind. Eng. Chem. Res.* **38**, 621–630.

Hui, K., Haff, J. E., Ungar, J. E. & Jackson, R. 1984 Boundary conditions for high-shear grain flows. *J. Fluid Mech.* **145**, 223–233.

Johnson, P. C. & Jackson, R. 1987 Frictional-collisional constitutive relations for granular materials, with application to plane shearing. *J. Fluid Mech.* **176**, 67–93.

Lee, J. 1994 Density waves in the flows of granular media. *Phys. Rev.* E **49**, 281–298.

Lee, J. S. & Leibig, M. 1994 Density waves in granular flow – A kinetic wave approach. *J. Phys. Paris* I **4**, 507–514.

Lun, C. K. K., Savage, S. B., Jeffrey, D. J. & Chepurniy, N. 1984 Kinetic theoreis for granular flow: inelastic particles in Couette flow and slightly inelastic particles in a general flow field. *J. Fluid Mech.* **140**, 223–256.

Lunt, E. M. 1992 *User's Manual for TNEK*, pp. 15–35. Program in Applied and Computational Mathematics, Princeton University.

Nakahara, A. & Isoda, T. 1997 $1/f^{\alpha}$ density fluctuation at the slugging transition point of granular flows through a pipe. *Phys. Rev.* E **55**, 4264–4273.

Nott, P. R., Alam, M., Agrawal, K., Jackson, R. & Sundaresan, S. 1999 The effect of boundaries on the plane Couette flow of granular materials: a bifurcation analysis. *J. Fluid Mech.* **397**, 203–229.

Nunziato, J. W. & Passman, S. L. 1980 Gravitational flows of granular materials with incompressible grains. *J. Rheol.* **24**, 395–420.

Peng, G. W. & Herrmann, H. J. 1994 Density waves of granular flow in a pipe using lattice-gas automata. *Phys. Rev.* E **49**, 1796–1799.

Peng, G. W. & Herrmann, H. J. 1995 Density waves and $1/f$ density-fluctuations in granular flow. *Phys. Rev.* E **51**, 1745–1756.

Richman, M. W. & Chou, C. S. 1988 Boundary effects on granular shear flows of smooth disks. *Z. Angew. Math. Phys.* **39**, 885–901.

Riethmuller, T., Schimanskygeier, L., Rosenkranz, D. & Poschel, T. 1997 Langevin equation approach to granular flow in a narrow pipe. *J. Statist. Phys.* **86**, 421–430.

Sanders, B. E. & Ackermann, N. L. 1991 Instabilities in granular chute flows. *J. Engng Mech. ASCE*, **117**, 2396–2406.

Sanders, B. E. & Ackermann, N. L. 1993 Microstrucutre in rapid gravity channel. *Mech. Mat.* **16**, 219–223.

Savage, S. B. 1979 Gravity flow of cohesionless granular materials in chutes and channels. *J. Fluid Mech.* **92**, 53–96.

Tan, M. L., Qian, Y. H., Goldhirsch, I., Orszag, S. A. 1995 Lattice-BGK approach to simulating granular flows. *J. Statist. Phys.* **81**, 87–103.

Wang, C.-H. 1995 Instabilities in granular materials flows. PhD dissertation, Princeton University.

Wang, C.-H., Jackson, J. & Sundaresan, S. 1997 Instabilities of fully developed rpaid flow of a granular material in a channel. *J. Fluid Mech.* **342**, 179–197.

Wang, C.-H. & Tong, Z. 1998 Transient development of instabilities in bounded shear flow of granular materials. *Chem. Engng Sci.* **53**, 3803–3819.

Zhang, D., & Foda M. A. 1997 An instability mechanism for the sliding motion of finite depth of bulk granular materials. *Acta Mechanica* **121**, 1–19.

https://doi.org/10.1017/S0022112001003792 Published online by Cambridge University Press